

Broadly versus Barely Variable Complex Chromophores of Planar Nickel(II) from κ^3 -*N,N',C* and κ^3 -*N,N',O* Donor Platforms

Riyadh Alrefai, Gerald Hörner, Hartmut Schubert, and Andreas Berkefeld*

Cite This: *Organometallics* 2021, 40, 1163–1177

Read Online

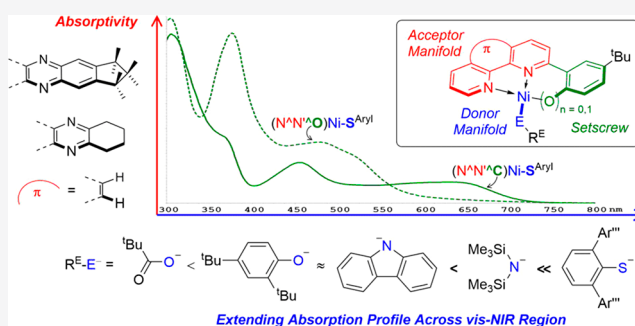
ACCESS |

Metrics & More

Article Recommendations

Supporting Information

ABSTRACT: This work reports on complex chromophores of planar nickel(II) of the general formula $[(\kappa^3\text{-}N,N',C/O)\text{Ni-ER}]$, which combines a κ^2 -*N,N'*-coordinate aromatic *N*-heterocycle with a pendant phenyl/phenol donor and the variable coligands ER (= carboxylato, phenolato, amido, and arylthiolato). The absorption properties of the planar complex chromophores vary broadly depending on the interplay of the three constituting components. Increasing the manifold of π^* -orbitals at the *N*-heterocyclic moiety through π -extension along 1,10-phenanthroline, tetrahydrodipyridophenazine, and dipyridophenazine has only a small impact on the energies of charge transfer type transitions across the visible (vis) to near-infrared (NIR) spectral region and is due to an inversion among spatially distinct but energetically close unoccupied molecular orbitals. Substantial absorptivity across the visible spectral region rather associates with the increasing capability among carboxylato, phenolato, amido, and arylthiolato coligands to engage in Ni–O/N/S π -bonding. This adds a mechanism for electronic coupling of coligand RE^- and π^* -orbitals at the *N*-heterocycle fragment through occupied d orbitals at nickel, enabling light-induced charge transfer. Aryl- S^- performs best in this regard, but $\{\text{Ni-O/N/S}\}$ -to-(*N*-heterocycle- π^*) charge transfer efficacy depends on donor–acceptor orbital alignment and appears to be kinetically hindered except for amido coligands owing to polar effects. Irrespective of the nature of coligand RE^- , the choice of the pendant phenyl/phenol side arm rules overall absorptivity by setting the energy of occupied frontier molecular orbitals.



INTRODUCTION

Exposing a chromophore system to light or a strong electric field is a common practice to make excited state energy available to chemical or physical processes. For use such as organic light-emitting diodes^{1–3} or photoredox catalysis,^{4–7} platinum group metal complexes from multidentate strong-field ligands are state-of-the-art chromophore systems owing to their general robustness, the efficient population of metal-to-ligand charge transfer triplet excited states (³MLCT) with lifetimes up to the microsecond time scale, and structural variability through ligand design.^{8–11} Alternatively, the population of excited d–d states can connect to useful photochemical properties for specific d electron configurations^{12–14} but generally presents a mechanism for nonradiative energy dissipation at unrivaled rates.

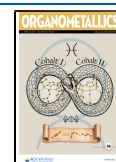
Strong σ -donor ligands contribute to increasing the lifetime of a potentially functional excited CT state by rendering excited d–d states and their population energetically less favorable.^{13,15–17} A conceptually related approach considers adjusting the energies of ligand π -donor orbitals to become either similar to or higher than those of metal d orbitals. Ligand–metal p–d π -bonding contributes to decreasing the energy gap between highest occupied and lowest unoccupied molecular orbitals, HOMO and LUMO, of the complex chromophore and thereby imparts absorptivity across the

visible-to-near-infrared (vis-to-NIR) spectral region.¹⁸ Originally considered for chromophore tuning of octahedral complexes of Fe(II)^{18,19} and other six-coordinate 3d metal ions including Ni(II),²⁰ we herein consider this concept for tailoring the properties of chromophore systems of planar Ni(II). Considering cyclometalated structures with strongly σ - and π -donating aryl ligands, precedent work in the field of planar complex chromophores of Ni(II) is limited to the κ^3 -*N,N,C*²¹ and κ^3 -*N,C,N*^{22,23} type frameworks depicted at the top of Scheme 1. Notably, the photophysical properties of planar bipyridine complexes of Ni(II) containing terminal aryl ligands have been studied in detail regarding their roles in light-promoted cross-coupling catalysis.^{7,24–26}

Building on our recent report on the selective κ^3 -*N,N',C*-cyclometalation of a 2-phenyl-1,10-phenanthroline platform by zero-valent Ni,²⁷ we herein focus on three parameters that govern the chromophore properties of this class of planar

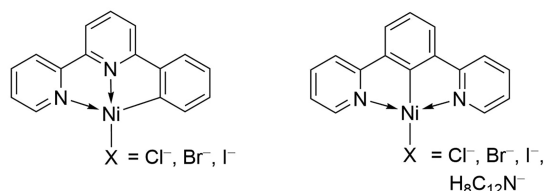
Received: March 2, 2021

Published: April 14, 2021

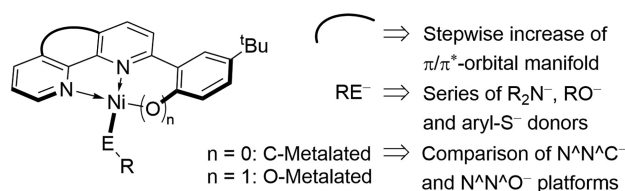


Scheme 1

Established strong-field complex chromophores of planar Ni(II):



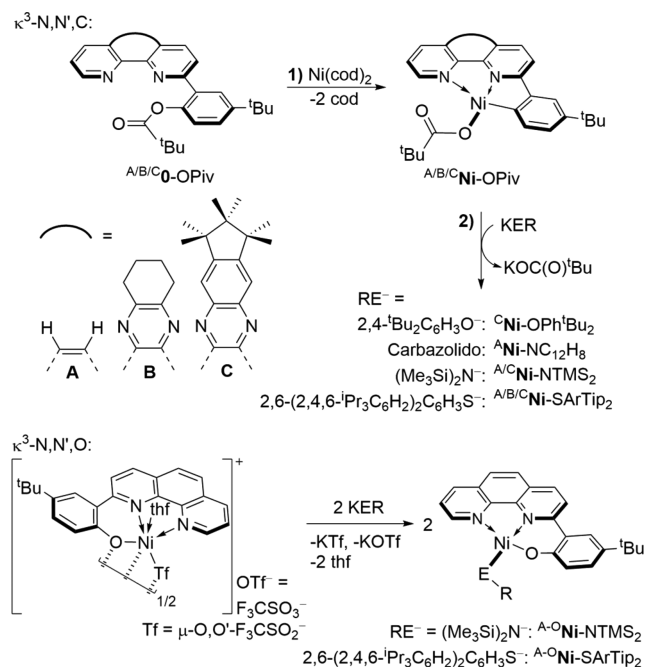
This work: Modulating ground-state vis-to-NIR absorption and redox properties through:



complexes as depicted at the bottom of Scheme 1. First, we focus on modulating the manifold of π^* -orbitals at the κ^2 - N,N' -bound N -heterocyclic backbone. Second, the effect of the Ni-ER fragment on ground-state absorption and redox properties is addressed. This parameter is relevant considering that 3d metal-carbazolido fragments can support photoluminescence.^{23,28} Third, making use of phenol-derived proligands has allowed us to compare the effects of κ^3 - N,N',C - versus κ^3 - N,N',O -cyclometalation on chromophore properties.

RESULTS

Preparation and Molecular Structures of Nickel Complex Chromophores. Scheme 2 provides an overview

Scheme 2. Preparation and Molecular Structures of Nickel Complex Chromophores^a

^aStructures of $^{A/A-O}$ Ni-NTMS $_2$ and A Ni-OPiv were reported previously.²⁷

of the preparation and molecular structures of Ni(II) complexes studied in this work. The conversion of 1,10-phenanthroline **A** into 10,11,12,13-tetrahydridiprido[3,2-*a*:2',3'-*c*]phenazine **B** and diprido[3,2-*a*:2',3'-*c*]phenazine **C** followed reported protocols,²⁹ and Scheme S1 provides the details. With regard to proligand preparation, we emphasize two modifications to the reaction conditions for the addition of the aryl side arm at the 3-position of frameworks **B** and **C** that have led to substantially improved yields. First, the reaction of the LiCl adducts of (tetrahydro)diprido[3,2-*a*:2',3'-*c*]phenazines **B** and **C**, preformed in THF, with 5-*tert*-butyl-2-methoxyphenyllithium improved conversions by a factor of ≥ 2 . Otherwise, yields of $\leq 30\%$ resulted as reported for related building blocks.²⁹ Second, the chemoselectivity for the oxidative rearomatization of the hydrolyzed products from aryllithium addition by excess MnO $_2$ correlates inversely with substrate concentration, so working in a dilute CH $_2$ Cl $_2$ solution is key to suppress the formation of substantial amounts of red colored byproducts. Notably, air suffices as oxidant in cases of backbone structures **B** and **C**.

Proligands $^{A/B/C}$ O-OPiv undergo selective metalation in toluene solution under ambient conditions, affording pivalato complexes $^{A/B/C}$ Ni-OPiv in 80–90% yield and analytical purity as brick red to red-brown crystalline solids. Ligand metathesis with potassium salts of the set of R_2N^- , aryl-O $^-$, and aryl-S $^-$ donors described in Scheme 2 led to products $^{A/B/C}$ Ni-ER that were isolated as crystalline solids. The κ^3 - N,N',O -type complex, $^{A-O}$ Ni-SArTip $_2$ (SArTip $_2 = 2,6$ -(2,4,6- t Pr $_3$ C $_6$ H $_3$) $_2$ C $_6$ H $_3$ S $^-$) was obtained in the form of dark red crystals in 82% yield following the protocol reported previously for $^{A-O}$ Ni-NTMS $_2$.²⁷

A general indication for C-metalation is the ^{13}C nuclear magnetic resonance (NMR) chemical shift of the Ni bound C atom that falls in the $147 \leq \delta_C \leq 150$ ppm range. The respective δ_C for phenolato complexes $^{A-O}$ Ni-ER locates at 162 ppm. The very low solubility of compounds $^{B/C}$ Ni-OPiv impaired recording ^{13}C NMR data, but transmission IR spectra in KBr show a diagnostic band at $\bar{\nu}(C=O) = 1612$ cm $^{-1}$ for the OPiv ligand akin to A Ni-OPiv, which corresponds to a redshift of 145 cm $^{-1}$ compared with the proligand phenol ester. Dipolar couplings in 1H - 1H NOESY and ROESY NMR data attest the relative spatial orientation of RE $^-$ with respect to the primary ligand such that a lone-pair np orbital at E orients toward the square coordination plane at nickel rather than the π -system of the N -heterocyclic moiety. The saturated 5- and 6-membered peripheral ring structures at the phenazine moieties of **C** and **B** were chosen to disfavor π -stacking and increase solubility, although this has had a counterproductive effect on obtaining detailed solid-state structure information from single-crystal X-ray diffraction (XRD) analysis that is available only for B Ni-OPiv. The solid-state molecular structures of B Ni-OPiv, A Ni-NC $_{12}$ H $_8$, and A Ni-SArTip $_2$ are depicted in Figure 1, and Figures S1 and S2 provide details for $^{A-O}$ Ni-SArTip $_2$ and a connectivity plot for C Ni-SArTip $_2$.

In all cases, the structure metrics agree with planar coordination at nickel and the relative alignment of the primary ligand and coligand RE $^-$ inferred from solution NMR data. Taking A Ni-NC $_{12}$ H $_8$ as an example, the coordination plane at nickel and the π -system of the carbazolido enclose an angle of 69 $^\circ$, confirming previously reported density functional theory (DFT)-derived structure metrics for an isomeric κ^3 - N,N',C -coordinate Ni(II) complex.²³ The bond geometry at the N atom of the carbazolido ligand is trigonal-planar akin to that

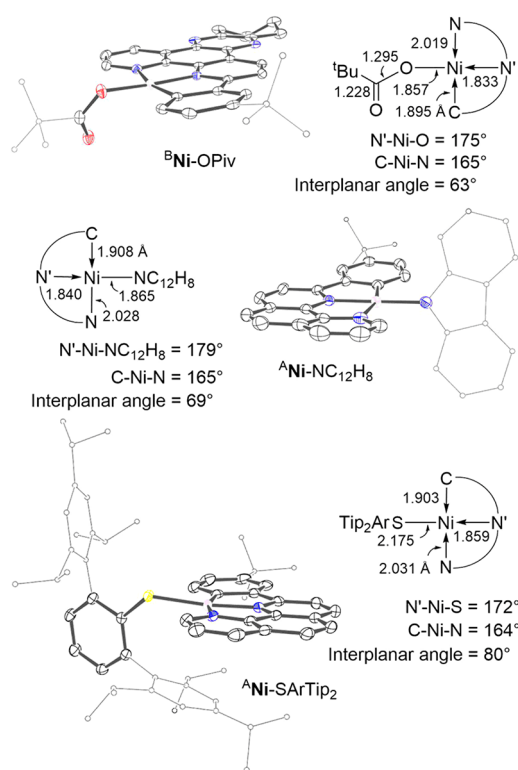


Figure 1. ORTEP plots and selected metrics for solid-state molecular structures of ^{A,B}Ni-ER, for RE⁻ = ^tBuC(O)O⁻ (top), H₈C₁₂N⁻ (center), and 2,6-(2,4,6-ⁱPr₃C₆H₂)₂C₆H₃S⁻ (bottom). The thermal displacement ellipsoids are set at 50% probability; H atoms are excluded for clarity.

of ^ANi-NTMS₂²⁷ but the smaller interplanar angle adopted in the solid-state structure of ^ANi-NC₁₂H₈ (69 vs 89° in ^ANi-NTMS₂) indicates that the lone-pair 2p orbital at N tilts toward the π-system of the phenanthroline backbone. The same applies to one of the lone-pair 3p orbitals at S in ^ANi-SARTip₂ that aligns perpendicularly with respect to the S-C(aryl) bond and thus tilts even further toward the π-system of the phenanthroline fragment. Experimental and computational data described further below indicate that the coplanar alignment of a lone-pair *np*-orbital at E and the π-system of the *N*-heterocyclic backbone is key to substantial chromophore absorptivity across the visible spectral region.

As noted in Figure 1, the Ni-N/N' bond lengths differ significantly in all structures owing to the trans influence of the strong aryl σ-donor. More notably, there is a distinct effect of RE⁻ on the Ni-N' bond length, shortened for carboxylate and carbazolidate and elongated for thiolate and the nonaromatic amide,²⁷ and may be rationalized by the different σ- and π-donor capabilities of the RE coligand. The distinct impact of RE⁻ on the redox and visible absorption properties is described in the following subsections.

Expanding the five-membered κ²-N',C-chelate ring moiety in ^ANi-ER to the six-membered κ²-N',O-moiety such as in ^{A-O}Ni-SARTip₂ has a strong impact on bond metrics. The six-membered chelate fragment appears to reduce geometric strain at Ni as the Ni-O bond is shorter by 0.09 Å compared to the Ni-C bond in ^ANi-SARTip₂. In turn, the Ni-N' and Ni-S bonds are elongated by 0.049 and 0.026 Å, respectively, very similar to the couple ^ANi-NTMS₂ and ^{A-O}Ni-NTMS₂ for which Δ*d*(Ni-N') = 0.054 Å and Δ*d*(Ni-NTMS₂) = 0.019

Å.²⁷ The coplanar alignment of the π-systems at the pendant aryl and the phenanthroline backbone found in ^ANi-ER diminishes slightly in ^{A-O}Ni-ER as the torsion angle about the C-C linkage increases from ~1 to ~7° in the thiolato and amido complexes.

Electronic Properties. Ultraviolet/Visible/Near Infrared (UV/Vis/NIR) Absorption Spectra. The UV/vis/NIR absorption spectra provide details as to the effects of the *N*-heterocyclic backbone, coligand RE⁻ and C- versus O-bonding of the pendant aryl side arm on chromophore properties. Starting with the impact of the *N*-heterocyclic backbone, the conversion of 1,10-phenanthroline **A** into 10,11,12,13-tetrahydrodipyrido[3,2-*a*:2',3'-*c*]phenazine **B** and fully aromatic congener **C** extends the manifold of π*-type acceptor MOs successively, and molar absorptivity in the near-UV and visible spectral regions parallels this order as exemplified for complexes ^{A/B/C}Ni-OPiv in Figure 2B. With regard to band

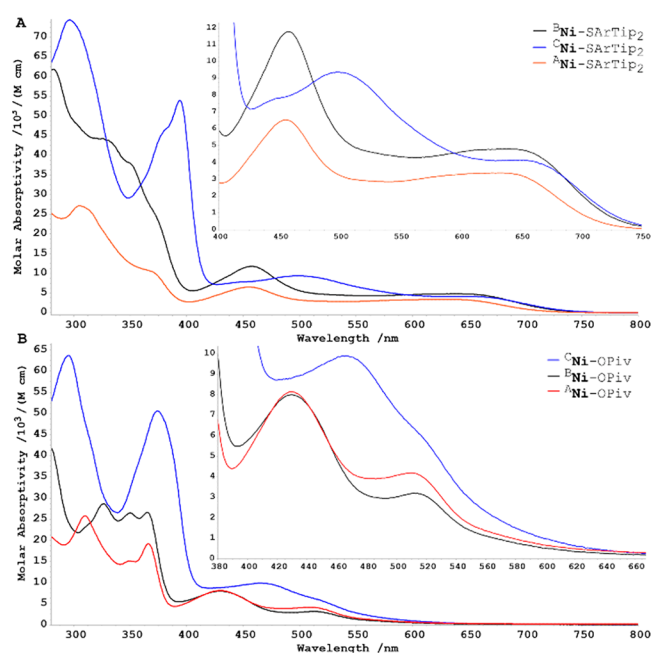


Figure 2. UV/vis/NIR absorption solution spectra (THF, 25 °C): (A) ^{A/B/C}Ni-SARTip₂, SARTip₂ = 2,6-(2,4,6-ⁱPr₃C₆H₂)₂C₆H₃S⁻, concentrations = 0.8–2.5 × 10⁻⁵ M; (B) ^{A/B/C}Ni-OPiv, OPiv = ^tBuC(O)O⁻, concentrations = 0.8–1.2 × 10⁻⁵ M.

energies, absorption profiles are almost congruent for ^{A/B}Ni-OPiv, whereas that for ^CNi-OPiv locates at lower energies. This trend is more pronounced for thiolato complexes ^{A/B/C}Ni-SARTip₂ as shown in Figure 2A. Contrary to the high-energy part of the visible spectral region at λ ≤ 500 nm that shows the same trend for band energies, band positions in the low-energy visible region for λ > 500 nm are remarkably similar within each series ^{A/B/C}Ni-ER with a given coligand RE⁻ as can be seen in the insets of Figure 2 for aryl-S⁻ and pivaloate and in Figure S3 for RE⁻ = TMS₂N⁻.

Comparing the absorption profiles for ^CNi-OPiv and ^CNi-SARTip₂ in Figure 2A,B attests to the pronounced effect of coligand RE⁻ on overall absorptivity of κ³-N,N',C-type chromophore systems in the visible spectral region. Taking a series of C-type ligand complexes as a representative example, the visible absorption profiles plotted in Figure 3 are similar for carboxylate (dotted black) and phenolate (solid brown), although ^CNi-OPh^tBu₂ exhibits an additional low-intensity

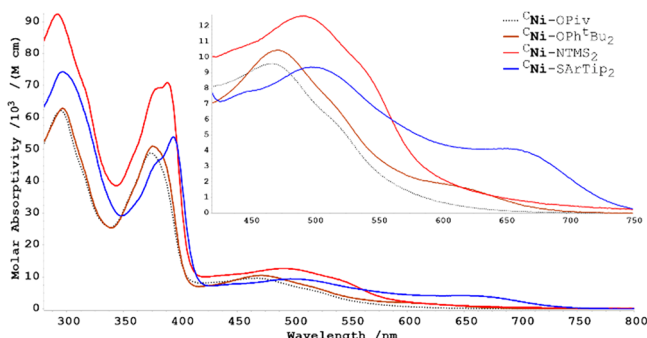


Figure 3. UV/vis/NIR absorption spectra (THF, 25 °C): ${}^{\text{C}}\text{Ni-ER}$, $\text{RE}^- = \text{OPiv}$ (${}^t\text{BuC}(\text{O})\text{O}^-$), OPh^tBu_2 ($2,4\text{-}{}^t\text{Bu}_2\text{C}_6\text{H}_3\text{O}^-$), NTMS_2 ($(\text{Me}_3\text{Si})_2\text{N}^-$), and SArTip_2 ($2,6\text{-}(2,4,6\text{-}{}^i\text{Pr}_3\text{C}_6\text{H}_2)_2\text{C}_6\text{H}_3\text{S}^-$). Concentrations = $0.7\text{--}1.1 \times 10^{-5}$ M.

band ($\epsilon \approx 1.5 \times 10^3 / (\text{M cm})$) that reaches the low-energy visible region at 600–700 nm as can be seen in the inset of Figure 3. Substitution for amide (solid red) results in an overall stronger absorptivity and a redshift of the absorption maxima. Similar to ${}^{\text{C}}\text{Ni-OPh}^t\text{Bu}_2$, ${}^{\text{C}}\text{Ni-NTMS}_2$ displays weak absorptivity in the 600–700 nm region. Finally, substitution for aryl-S- leads to an absorption profile (solid blue) that spans the visible region for all complexes ${}^{\text{A/B/C}}\text{Ni-SArTip}_2$ as shown in Figures 2 and 3.

The overall picture for C-type chromophores applies likewise to their A-type congeners. Substitution of the nonaromatic amide in ${}^{\text{A}}\text{Ni-NTMS}_2$ for carbazolidone results in a shift of the visible absorption profile to higher energies as shown in Figure S3. Notably, ${}^{\text{A}}\text{Ni-NC}_{12}\text{H}_8$ exhibits a high-energy visible band at 430 nm that is reminiscent of pivaloate complexes ${}^{\text{A/B}}\text{Ni-OPiv}$, shown in Figure 2. In contrast to ${}^{\text{A/B}}\text{Ni-OPiv}$, ${}^{\text{A}}\text{Ni-NC}_{12}\text{H}_8$ absorbs up to 700 nm, albeit at ~ 4 times lower intensity compared with ${}^{\text{A/B}}\text{Ni-SArTip}_2$. Overall, it is the π -donor capability of coligand RE^- and its relative alignment toward the N-heterocycle π^* -orbitals that relates to absorptivity in the low-energy visible spectral region, whereas a lower impact results for high-energy visible bands that depend primarily on the type of N-heterocyclic moiety.

In stark contrast to the variable absorption properties of aryl-metalated chromophores ${}^{\text{A/B/C}}\text{Ni-ER}$, visible absorption profiles of phenol congeners ${}^{\text{A-O}}\text{Ni-SArTip}_2$ and ${}^{\text{A-O}}\text{Ni-NTMS}_2$ ²⁷ differ primarily in terms of molar absorptivity. As shown in Figure 4, the UV and visible light absorption profile of ${}^{\text{A-O}}\text{Ni-SArTip}_2$ (solid line) is very similar to that of ${}^{\text{A-O}}\text{Ni-NTMS}_2$ (dotted line), and both exhibit only weak absorptivity

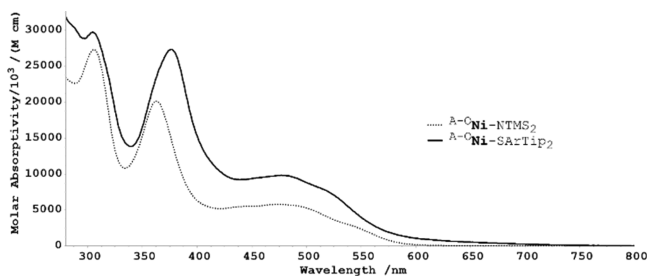


Figure 4. UV/vis/NIR absorption spectra (THF, 25 °C): ${}^{\text{A-O}}\text{Ni-SArTip}_2$ (solid line; $\text{SArTip}_2 = 2,6\text{-}(2,4,6\text{-}{}^i\text{Pr}_3\text{C}_6\text{H}_2)_2\text{C}_6\text{H}_3\text{S}^-$) and ${}^{\text{A-O}}\text{Ni-NTMS}_2$ (dotted line; included for comparison).²⁷ Concentrations $\leq 3.0 \times 10^{-5}$ M.

in the low-energy visible region toward 700 nm. The marked reduction of absorptivity in the vis-to-NIR region for chromophores ${}^{\text{A-O}}\text{Ni-ER}$ indicates a substantial impact of the pendant aryl/phenol donor on the energy of frontier MOs.

The variation of visible band energies on solvent polarity attests their charge transfer (CT) character and associates with a decrease of the permanent dipole moment upon going from the ground state to the electronically excited state. Taking ${}^{\text{C}}\text{Ni-SArTip}_2$ as an example, the band at lowest energy blue-shifts by $\sim 1000 \text{ cm}^{-1}$ upon substituting pentane ($\lambda_{\text{max}} = 690 \text{ nm}$) for thf ($\lambda_{\text{max}} = 654 \text{ nm}$) and 1,2-difluorobenzene ($1,2\text{-C}_6\text{H}_4\text{F}_2$; $\lambda_{\text{max}} = 647 \text{ nm}$) as shown in Figure 5. The high-energy visible band,

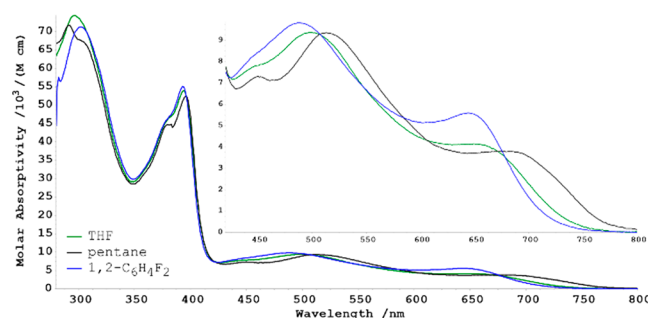


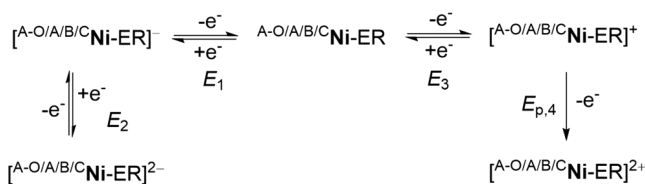
Figure 5. UV/vis/NIR absorption spectra (solvents as indicated, 22 °C): ${}^{\text{C}}\text{Ni-SArTip}_2$, $\text{SArTip}_2 = 2,6\text{-}(2,4,6\text{-}{}^i\text{Pr}_3\text{C}_6\text{H}_2)_2\text{C}_6\text{H}_3\text{S}^-$. Concentrations = $8.2\text{--}8.7 \times 10^{-6}$ M.

observed at 500 nm in thf solution, is similarly affected, whereas a negligible shift results for the bands at $\lambda \leq 400 \text{ nm}$, which points to electronic transitions between delocalized sets of MOs in the near-UV. Figure S4 compares UV–vis–NIR absorption profiles for the series of complexes ${}^{\text{A/B/C}}\text{Ni-SArTip}_2$ recorded in THF and in 1,2-difluorobenzene solutions. The negative solvatochromism found for the high-energy visible bands in the 400–500 nm region (cf. inset, Figure S4) increases noticeably along $\text{A} < \text{B} < \text{C}$, in particular in the transition from B to C. In other words, the change of the ground-state permanent dipole moment that associates with the CT transition(s) in the high-energy visible region is largest for ${}^{\text{C}}\text{Ni-SArTip}_2$.

Emission Spectroscopy. Compounds ${}^{\text{A}}\text{Ni-NC}_{12}\text{H}_8$, ${}^{\text{A/A-O}}\text{Ni-NTMS}_2$, and ${}^{\text{A/A-O}}\text{Ni-SArTip}_2$ have been chosen to address the emission properties of this class of nickel complex chromophores. Neither of the chromophores luminesces in dilute ($\leq 50 \mu\text{M}$) 2-Me-thf solution (293 K) and glass (77 K) upon excitation of the CT bands in the visible region or the $\pi\text{-}\pi^*$ -type transitions in the near-UV. The same applies to the crystalline materials when irradiated by an UV lamp. Irradiation at $\lambda_{\text{rad}} = 265 \text{ nm}$ stimulated the appearance of a very weak emission band at $\lambda_{\text{em}} \approx 350 \text{ nm}$ (and its second harmonic at $\sim 700 \text{ nm}$) as depicted in Figure S12. This emission appears to relate to a metal ion impurity and/or defect structure in the borosilicate glass of the sample tubes because it is strongly reduced in quartz glassware under otherwise identical conditions.

Cyclic Voltammetry (CV). Scheme 3 provides an overview of the redox processes supported by compounds ${}^{\text{A-O/A/B/C}}\text{Ni-ER}$ as determined by CV, and Table 1 displays the pertinent data.

First, all complexes undergo two reduction events within the cathodic potential limit of the electrolyte medium, that is ca. -2.72 V vs the ferrocene/ferrocenium couple (V vs Fc/Fc^+).

Scheme 3. Redox Processes of Complexes $A-O/A/B/CNi-ER$ 

The first reduction is electrochemically reversible in all cases, and E_1^0 values vary by ≤ 0.35 V between *N*-heterocyclic moieties A and C. For $RE^- = \text{aryl-S}^-$, E_1^0 values are very similar for backbones A and B, whereas a shift of ~ 0.25 V to more positive potentials is found for C. An equivalent picture results for the couple of amido complexes $^ANi-NTMS_2$ and $^CNi-NTMS_2$. As to the impact of coligand RE^- on E_1^0 , two subclasses can be differentiated: (a) the weak and moderate π -donors pivalate (carboxylate) and carbazolidine and (b) the stronger π -donors $(Me_3Si)_2N^-$ and aryl-S^- . A higher π -donor capability appears to render reduction thermodynamically less favorable, with $\Delta E_1^0 \leq 0.07$ V for C-type and $\Delta E_1^0 \geq 0.15$ V for A-type backbones. According to computational data described further below, the lower impact of coligand RE^- on E_1^0 in case of backbone C results from the inversion of energetically close LUMO and LUMO+1 that associates with the transition from A/B to C.

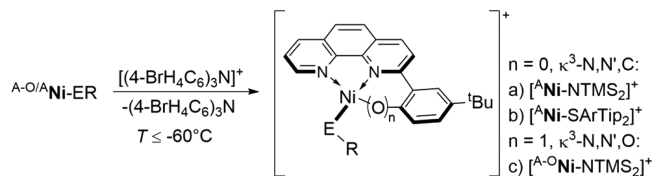
Contrary to the first reduction, the second reduction event is electrochemically reversible at $\nu \leq 1000$ mV s $^{-1}$ for (tetrahydro)phenazine platforms B and C only, and E_2^0 correlates with the sizes of their π -manifolds as can be seen from comparing the first three entries of Table 1. According to the computational data reported below, the electrochemical reversibility associates with the localization of the two electrons in spatially different and electronically weakly coupled acceptor π -orbitals in case of B and C.

The second general property is that all complexes can be oxidized at least once up to the high potential limit, ~ 1.7 V, of the electrolyte medium. Most notably, only the amido complexes support electrochemically reversible oxidation, and E_3^0 values for $^ANi-NTMS_2$ and $^ANi-NC_{12}H_8$ differ by 20 mV. Electrochemically irreversible oxidation prevails otherwise, irrespective of the type of *N*-heterocycle A–C and the pendant C-/O-aryl group, although peak potentials E_3 are remarkably similar for the O- and S-coligands. Electrochemical irrever-

sibility disallows quantitative comparisons, but the shift of E_3 to more positive potentials for increasing potential sweep rates and sample concentrations indicates that heterogeneous electron transfer is rate-limiting, which points to a critical effect of RE^- on electronic relaxation during the electron transfer to and from the electrode. An irreversible chemical reaction that withdraws the electrochemically generated complex cation from its Nernst equilibrium would result in the opposite trend of E_3 .³⁰ Further oxidation to complex dicationations either is electrochemically irreversible or may occur at potentials more positive than the limit supported by the electrolyte medium for complexes from the C-type ligand framework.

The third general property considers the effect of the bonding mode of the pendant aryl donor on reduction potential E_1^0 and oxidation potential E_3 . The apparent minor impact of the pendant C-/O-aryl on E_1^0 attests that reduction is confined to π^* -orbitals at the *N*-heterocyclic backbone. Such an electronic compartmentalization agrees with a combined electrolysis/cw-EPR and DFT study of $[(\kappa^3-N,N',C)Ni-Cl]$ complexes from a 2,2'-bipyridine type ligand platform.²¹ With regard to oxidation, O-bonding associates with an anodic shift of E_3 by ≥ 0.3 V irrespective of RE^- and indicates a substantial contribution of the phenolato fragment to the HOMO of $A-O-Ni-ER$.

Characterization of Radical Cation Complexes. Complexes $^ANi-NTMS_2$, $A-O-Ni-NTMS_2$, and $^ANi-SArTip_2$ have been chosen as representative examples to further address the distinct effects of C-/O-bonding and coligand RE^- on redox properties. As described by Scheme 4, stoichiometric oxidation

Scheme 4. Chemical Oxidation of $A-O/A-Ni-ER$ 

with $[(4-BrH_4C_6)_3N]BAR_4^F$ [$BAR_4^F = (3,5-(F_3C)_2C_6H_3)_4B^-$] at $T \leq -60$ °C in 1:1 toluene/ CH_2Cl_2 and CH_2Cl_2 solutions afforded complex cations for X-band cw-EPR (Figures S6–S11) and UV/vis/NIR absorption spectroscopic analysis

Table 1. Redox Potentials from CV^a

backbone	RE^-	E_1^b	E_2^b	E_3^b	$E_{p,4}^b$
A	Tip_2ArS^-	-2.06	-2.71 (ir)	0.08–0.11 (ir)	0.20 (ir)
B	Tip_2ArS^-	-2.00	-2.53	0.09–0.11 (ir)	0.22–0.26 (ir)
C	Tip_2ArS^-	-1.75	-2.32	0.04–0.11 (ir)	
C	tBu_2PhO^-	-1.73	-2.24	0.07–0.10 (ir)	
C	TMS_2N^-	-1.73	-2.29	0.08	
C	$PivO^-$	-1.68	-2.17	0.09–0.13 (ir)	
A	$PivO^-$	-1.91	-2.62 (ir)	0.07 (ir)	0.39 (ir)
A	$H_8C_{12}N^-$	-1.92	-2.55 (ir)	0.07	0.81 (ir) ^c
A	TMS_2N^-	-2.08		0.05	
O–A	TMS_2N^-	-2.06 ^d		0.36	1.01 (ir)
O–A	Tip_2ArS^-	-1.97 (qr) ^{d,e}	-2.28 (ir)	0.30 (ir)	≥ 0.78 (ir) ^f

^aConditions: glassy carbon working electrode, 0.1 M $nBu_4NPF_6/1,2$ -difluorobenzene electrolyte solution, $T = 20$ °C, $50 \leq \nu \leq 2000$ mV/s. ^b E (V vs Fc/Fc^+); ir/qr = electrochemically irreversible/quasireversible, E_p at $\nu = 100$ mV/s. ^cA third irreversible oxidation occurs at $E_p(100$ mV/s) = 1.04 V. ^dUpon reversal of scan direction, the wave for reoxidation is broadened at all scan rates. ^eReduction induces a follow-up reactivity leading to another oxidation event at $E_{p,ox} = -0.65$ V. ^fA series of ill-defined oxidation events is observed.

(Figure S5). Table 2 lists the principal values of g tensors and hyperfine coupling $A(^{14}\text{N}, I = 1, 99.64\%)$.

Table 2. X-Band cw-EPR Spectroscopic Parameters of Complex Cations $\text{A}^{-\text{O}}/\text{A}^{\text{Ni-ER}}^{\text{a}}$

precursor	g_x, g_y, g_z^b	g_{iso}^c	A_x, A_y, A_z^d
	2.110 [0.018]		n.r.
$\text{A}^{\text{Ni-NTMS}_2}$	2.066 [0.011]	2.068 [2.068]	58
	2.028 [0.010]		n.r.
	2.046 [0.005]		n.r.
$\text{A}^{-\text{O}}\text{Ni-NTMS}_2$, minor product, I	2.026 [0.005]		n.r.
	2.015 [0.003]	2.031	n.r.
	2.057 [0.015]	[I, 2.029; II, 2.034]	n.r.
$\text{A}^{-\text{O}}\text{Ni-NTMS}_2$, major product, II	2.043 [0.006]		n.r.
	2.002 [0.003]		n.r.
	2.272 [0.017]		
$\text{A}^{\text{Ni-SArTip}_2}^e$	2.099 [0.018]	[2.141]	
	2.052 [0.009]		

^aConditions: 1/1 toluene/ CH_2Cl_2 , glass (100 K) and solution (213 K), oxidant = $[(4\text{-BrC}_6\text{H}_4)_3\text{N}]\text{B}(3,5\text{-}(\text{F}_3\text{C})_2\text{C}_6\text{H}_3)_4$, $T = -78$ °C. ^bDistribution of principal g values represented by the “ $g\text{Strain}$ ” parameter used in EasySpin³¹ given brackets. ^c $[g_{\text{iso}} = 1/3(g_x + g_y + g_z)]$ from EPR data at 100 K. ^d $A(^{14}\text{N}, I = 1, 99.64\%)$ in MHz; n.r. = not resolved. ^eSpectrum (Figure S11) shows an additional set of resonances of a minor $S = 1/2$ species.

Rhombic g tensors prevail in all three cases, and the principal g values exceed the free electron g value $g_e \approx 2.003$, indicating a variable admixture of Ni-borne orbitals to the singly occupied frontier MO (SOMO). On the basis of simulations of EPR spectra depicted in Figures S6 and S8, oxidized $\text{A}^{\text{Ni-NTMS}_2}$ is best described as a nickel-amidyl radical complex cation with unpaired electron density locating primarily in an N 2p orbital. Similar to a Rh-amidyl radical cation,³² location of spin density in a p orbital relates to the distinct anisotropy and small size of principal A values, which in this case indicates orientation of A_y along the N 2p orbital that likely orients along the coordination plane at Ni. Considering A_y as the only resolved principal hyperfine component allows reproducing the distinct curvature of the central derivative line depicted in Figures S6 and S8. Each of the principal g components shows a significant distribution in frozen solution that is attributed to a distribution of interplanar angles enclosed by the putatively trigonal amidyl-radical fragment and the primary ligand framework and affects π -type Ni-NTMS₂ 3d-2p orbital overlap. Warming the sample to 213 K results in a broadened and featureless derivative line (cf. Figure S7) that persists upon further warming to ambient temperatures.

Monitoring the oxidation of $\text{A}^{\text{Ni-NTMS}_2}$ at -60 °C by UV/vis/NIR absorption spectroscopy corroborated the formation and persistence of the complex amidyl-radical cation. In line with the aforementioned influence of coligand RE^- on the individual bands in the visible spectral region, the intensity of the high-energy visible band of the starting material markedly decreased, whereas the low-energy visible band disappeared in favor of an intense band that locates at even lower energy as depicted in Figure S5. The occurrence of the low-energy band points to a putative CT transition from a lower lying occupied MO into the SOMO that derived from the former HOMO. Overall, the marked attenuation of absorptivity in the high-energy visible region combines with intense absorption at

lower energy to result in the emerald green color of the Ni-amidyl radical complex cation.

Amido ligand centered oxidation was further corroborated by using 1,1'-diacetylferrocenium bis(trifluoromethanesulfonyl)imide, $[\text{Fc}^{\text{II}}]\text{NTf}_2$, as the oxidant. In addition to the amidyl-radical complex cation, a Ni(III) complex forms as a minor coproduct ($\sim 10\%$) with $g_x = 2.434$ and $g_y = 2.307$, while g_z is masked by the resonances of the Ni-amidyl radical cation as can be seen in Figure S8. Assuming $g_x \approx g_y \gg g_z$ equals the order reported for complexes of 5- and 6-coordinate Ni(III)³³⁻³⁶ and is herein attributed to O-bonding of the $(\text{F}_3\text{CSO}_2)_2\text{N}$ -counterion. The emerald green Ni-amidyl radical cation converts into a yellow, EPR-silent product or mixture of products at ambient temperature but on distinct time scales depending on the counterion, namely, minutes for NTf_2 and hours for the weakly coordinating borate.

Contrary to the selective oxidation of $\text{A}^{\text{Ni-NTMS}_2}$ in the presence of weakly coordinating borate, oxidation of $\text{A}^{-\text{O}}\text{Ni-NTMS}_2$ with $[(4\text{-BrH}_4\text{C}_6)_3\text{N}]\text{BARF}_4$ led to a mixture of two products that adopt a $\sim 1:1.5$ ratio according to EPR spectra acquired at 100 K as shown in Figure S9. We attribute the minor component to the product from oxidation of the primary ligand, namely, $[(\kappa^3\text{-N,N',O}^{\bullet})\text{Ni}(\text{NTMS}_2)]^+$, and the major component to the product from oxidation of the amido ligand, namely, $[(\kappa^3\text{-N,N',O}^-)\text{Ni}(\text{NTMS}_2)]^+$. Different from oxidized $\text{A}^{\text{Ni-NTMS}_2}$, hyperfine splitting is not resolved for any of the three components of the A tensors of either redox isomer, and the anisotropies of g tensors are much smaller. Assuming that fragment rotation about the Ni-N bond to the amidyl-radical is less restricted than about the Ni-O bond to the rigid primary ligand, we assign the Ni-phenoxy radical cation to the g tensor with the narrower distribution of principal components. At 213 K, the subspectra collapse into a single broad derivative line shown in Figure S10, with g_{iso} being equal to the weighted average calculated from $g_{\text{iso,I}}$ and $g_{\text{iso,II}}$, which points to the rapid interconversion of the redox isomers on the experimental time scale. Same as for oxidized $\text{A}^{\text{Ni-NTMS}_2}$, oxidation products from $\text{A}^{-\text{O}}\text{Ni-NTMS}_2$ convert gradually into an EPR silent product or mixture of products within hours at room temperature.

Oxidation of $\text{A}^{\text{Ni-SArTip}_2}$ at -78 °C affords a red-brown solution that changes color instantaneously to yellow and finally green upon warming to ambient temperature. EPR spectra at 100 K point to the formation of two products as depicted in Figure S11. The major product is characterized by a g tensor with $g_x \gg g_y, g_z$ that each shows substantial distribution, pointing to a shallow potential well for rotational motion about the Ni-S bond akin to $\text{A}^{\text{Ni-NTMS}_2}$. We attribute the marked deviation of one of the principal components of the g tensor from g_e to the localization of spin density in a 3(d-p) Ni-S π -bond, which implies a partially covalent character of named bond also in parent complexes $\text{A}^{\text{B/C}}\text{Ni-SArTip}_2$. The g tensor for the minor component cannot be fully deduced but anisotropy appears much smaller and suggests a diminished 3(d-p) Ni-S π -bond character. We therefore tentatively assign the minor component to a complex nickel-thiyl radical cation in which the aryl-S fragment adopts an obtuse interplanar angle such that spin-density localizes predominantly at sulfur. In line with this description, EPR spectra recorded at 213 K appear to consist of an extremely broadened derivative line that hardly distinguishes from the baseline. Further warming of the sample

inside the microwave cavity to room temperature caused instantaneous and irreversible degradation.

Computational Data. Structures of complexes $A-O-Ni-ER$ and $A/B/C-Ni-ER$ for coligands $RE^- = OPiv, NC_{12}H_8, NTMS_2,$ and $SArTip_2$ have been optimized with density functional theory (DFT) methods using the BP86 functional. Details of the computational settings can be found in the [Experimental Section](#). In addition, $[A-O/A/B/C-Ni-S^tBu]^{+/0/-/2-}$ and $A-O/A/B/C-Ni-SArMe_2$, with $Me_2ArS^- = 2,6-(H_3C)_2C_6H_3S^-$, have been optimized as truncated models of $A-O/A/B/C-Ni-SArTip_2$. Predicted metrics have been calibrated with experimental data. An excellent match is generally observed, except for the artificially elongated Ni–N bond located trans to the Ni–C bond. Reference calculations with the Ni–N bond length constrained to the experimental value resulted in marginal energy differences. Pertinent metrical data is provided in [Tables S1–S3](#). EPR parameters of cations $[^ANi-NTMS_2]^+, [^A-O-Ni-NTMS_2]^+,$ and $[^ANi-SArTip_2]^+$ were calculated using the B3LYP functional. Frontier MO diagrams and related electronic properties were addressed in single-point calculations with the TPSSh functional as established in previous work on planar Ni(II) complexes.^{22,27,37}

We first focus on the impact of coligand RE^- on the electronic structure in ^ANi-ER ; equivalent conclusions hold for derivatives of **B** but not for **C**. Kohn–Sham frontier MOs are depicted in [Figure 6](#).

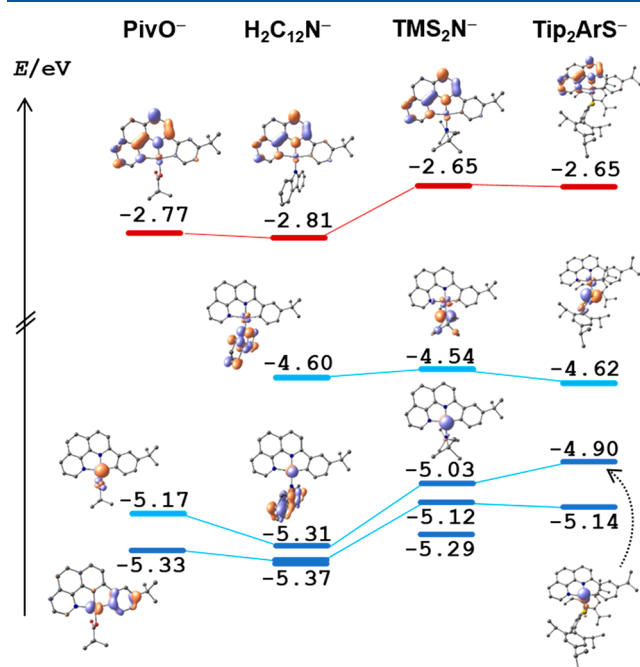


Figure 6. DFT-derived Kohn–Sham frontier MOs (TPSSh-D3/TZVP level of theory). Effect of coligand RE^- on the energetic order and the character of ^ANi-ER . Occupied MOs, blue; virtual orbitals, red.

Evidently, the nature of RE^- does not affect the character of the LUMO that is centered at the κ^2-N,N' -bipyridine moiety in all cases, albeit it modulates the energy by up to 150 mV. In agreement with electrochemical data, the range of LUMO energies coincides with the RE-dependent variation of E^0_1 given in [Table 1](#). The computed divergence of LUMO energies reproduces the phenomenological categories of carboxylate and carbazolidate as weak/moderate and TMS_2N^- and aryl- S^- as

strong π -donor ligands. However, the character of the HOMO is subject to qualitative change when RE^- is varied. The highest donor orbital is clearly metal-borne (d_{z^2}) in $^ANi-OPiv$, as has been found previously.²⁷ MOs of Ni–O(Piv) 3d–2p π -bond character are highly stabilized, $E < -6$ eV, and do not contribute to the frontier MOs. In consequence, oxidation of $^ANi-OPiv$ is expected to be nickel-centered, and it is noted that DFT-optimization of $[^ANi-OPiv]^+$ involves κ^2-O,O' -OPiv bonding, which stabilizes Ni(III) by increasing the coordination number. The presence of nominally stronger π -donor coligands introduces MOs of Ni–E 3d–2/3p π -bond character at far more positive energy, rendering them accessible to optical and electrochemical techniques. In $^ANi-NTMS_2$, $^ANi-NC_{12}H_8$, and $^ANi-SArTip_2$ (and respective models $^ANi-SArMe_2$ and $^ANi-S^tBu$) the HOMO indeed manifests largely as a 2/3p orbital localized on E, featuring π -antibonding interactions with a Ni d_{xy} orbital. Oxidation of these complexes is expected to be ligand centered, as is found in experiment. DFT-derived EPR parameters for $[^ANi-NTMS_2]^+$ and $[^ANi-SArTip_2]^+$ ([Table S7](#)) corroborate the distinct anisotropy of g tensors found experimentally, lending strong support to the DFT assignment of the donor orbitals.

We next turned to the effects of the manifold of π -orbitals at the N -heterocyclic moiety, using $A/B/C-Ni-S^tBu$ as a representative model for $A/B/C-Ni-SArTip_2$. Frontier MOs for the series are shown in [Figure 7](#), and very similar results are obtained all across the RE^- substitution series.

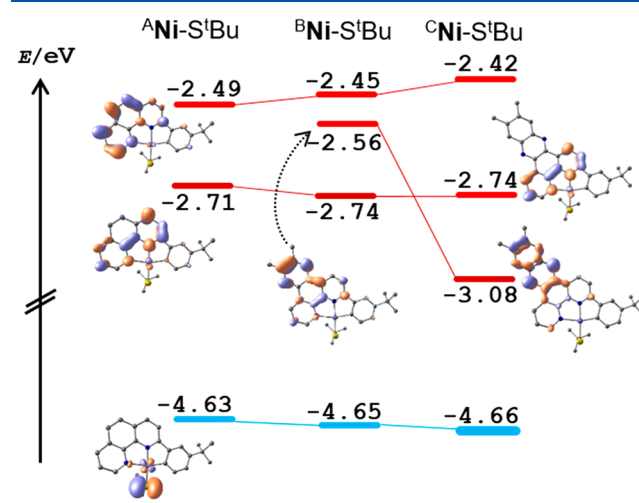


Figure 7. DFT-derived Kohn–Sham frontier MOs (TPSSh-D3/TZVP level of theory). Effect of π -extension on energetic order and character of $A/B/C-Ni-S^tBu$. Occupied MOs, blue; virtual orbitals, red.

As expected, the donor levels are hardly affected by the expansion of the π -system from **A** to **C**. Intriguingly, also the overall appearance of the acceptor levels is largely unaffected. For **A**, they are centered at the κ^2-N,N' -bipyridine moiety and are energetically close ($E = -2.71$ and -2.49 eV), and for **C**, they change marginally ($E = -2.74$ and -2.42 eV). Expansion of the N -heterocyclic π -system adds qualitatively new donor levels to the MO diagram at $E = -2.56$ and -3.08 eV for **B** and **C**, respectively. In consequence, the first reduction event localizes at the κ^2-N,N' -bipyridine fragment in **A** and **B** at very similar potentials, whereas a phenazine-centered reduction is favored by ~ 0.3 V in case of **C** owing to an inversion of the LUMO character. Computed Mulliken spin densities of the

anions $[\text{A/B/CNi-S}^t\text{Bu}]^-$, included in Figure S13, visualize the qualitative difference between **B** and **C** as they stand for the contrasting character of the parent LUMO. The second reduction step of **B** and **C** yields triplet dianions with an integer spin residing both in the phenazine and the phenanthroline moiety. Evidently there is only minor electronic communication among both moieties, allowing for the reversible storage/donation of two electrons in electronically distinct sections of a single acceptor ligand.

Having established level-crossing in the electrochemically addressable acceptor orbitals between **B** and **C**, it is intriguing to recall the experimental vis/NIR spectra of series A/B/CNi-SArTip_2 in Figures 2 and 3. According to the absorption spectra, both the energy and the intensity of the lowest-energy transitions around 650 nm hardly respond to the nature of the π -system of the *N*-heterocyclic backbone. This finding is commensurate with the MO diagram shown in Figure 7 only if the electroactive LUMO of **C** is not involved in the diagnostic low-energy transition. Instead, the low-energy bands are best interpreted as CT transitions between thiolate-borne donor levels and phenanthroline centered π^* -orbitals, namely, the LUMO for **A** and **B** and LUMO+1 for **C**. This assignment is corroborated by the decent match of the experimental vis/NIR band energies and the HOMO–LUMO(+1) gaps, which amount to ~ 2.0 eV. Similar interpretations hold for the spectra of amides A/B/CNi-NTMS_2 . The transitions at longest wavelengths here are likewise independent of the extent of the *N*-heterocycle π -manifold, featured as weak shoulders ($\epsilon < 1000/\text{(M cm)}$) at ca. 600 nm, again in agreement with the vertical HOMO–LUMO(+1) gap as depicted in Figure S15. This change of the nature of the acceptor orbital from LUMO to LUMO+1 for increasing π -extension of the *N*-heterocyclic moiety and the associated invariability of lowest-energy electronic transitions are reminiscent of the behavior reported for planar complexes $[(\kappa^3\text{-N,Amido,N})\text{Ni-Cl}]$ from a series of phenanthridine-containing ligands.³⁸

Closer inspection of the orbitals involved in the optical transitions hints to the origin of the massive intensity difference of $\sim 1:4$ between the HOMO–LUMO(+1) transitions of the series of amido and thiolato complexes. These very transitions are forbidden by symmetry both in the amides and the thiolates, due to the (almost) orthogonal donor and acceptor arrangement in the optimized structures, rendering the transitions silent in TD-DFT. Rotation about the Ni–E bond will lift these limitations, and it is tempting to ascribe the recovered intensity of a symmetry-forbidden transition to the rotation about the Ni–S bond in A/B/CNi-SArTip_2 . Indeed, the existence of rotamers was inferred as the source of speciation in solution-phase EPR spectra. The rotamer hypothesis was tested using $\text{A}^{\text{Ni-SArMe}_2}$ as a truncated model for $\text{A}^{\text{Ni-SArTip}_2}$; the structures are given in Figure S16. Optimization of $\text{A}^{\text{Ni-SArMe}_2}$ gave two close-to-degenerate minima, for which rotation aligns the *N*-heterocyclic π -system coplanar with an antibonding Ni–S 3d–3p π -type orbital combination. Accordingly, TD-DFT computation gave intense vis–NIR transitions for both rotated species. The validity of the argument was cross-checked through TD-DFT analysis of a constrained structure of $\text{A}^{\text{Ni-SArMe}_2}$, with orthogonally fixed Ni–S–Ar constellation, akin to the global minima of $\text{A}^{\text{Ni-SArTip}_2}$ and $\text{A/B/CNi-S}^t\text{Bu}$. In keeping with the rotamer hypothesis, orthogonally constrained $\text{A}^{\text{Ni-SArMe}_2}$ gives no intense vis–NIR transitions.

Finally, we addressed the substantial impact of O-bonding on chromophore properties of $\text{A}^{\text{O-Ni-SArTip}_2}$ and $\text{A}^{\text{O-Ni-NTMS}_2}$. While the character of the LUMO and the Ni–S 3d–3p π -bond nature of the HOMO are conserved in $\text{A}^{\text{O-Ni-ER}}$, the corresponding stabilization of the HOMO inferred from electrochemical and electronic absorption data is quantitatively echoed in a DFT-derived MO diagram shown in Figure 8.

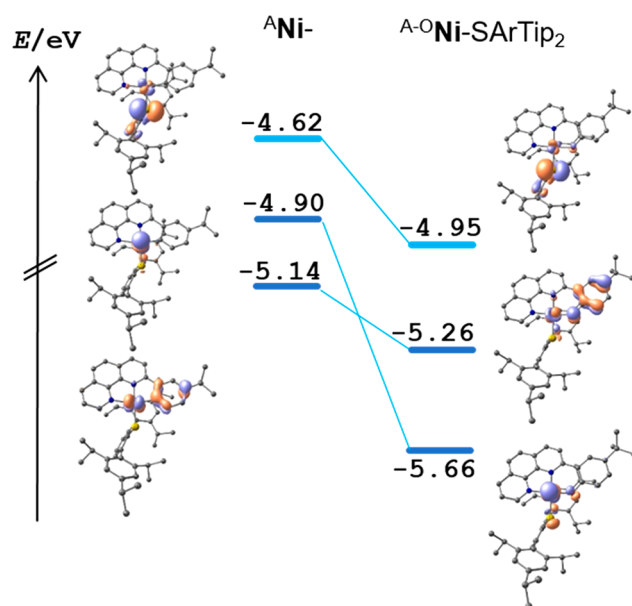


Figure 8. DFT-derived Kohn–Sham frontier MOs (TPSSH-D3/TZVP level of theory). Effect of C-/O-metalation on energetic order and character of HOMO–*n*, *n* = 0–2, for $\text{A}^{\text{O/A}^{\text{Ni-SArTip}_2}$.

The increasing HOMO–LUMO gap derived from DFT data explains the experimentally observed confinement of absorptivity to the high-energy visible region. In general, spectra from series $\text{A}^{\text{O-Ni-ER}}$ are much less prone to donor-dependent variation than the spectra of parent series $\text{A}^{\text{Ni-ER}}$.

DISCUSSION

The lack of luminescence for $\text{A}^{\text{Ni-NC}_{12}\text{H}_8}$ and its congeners contrasts reported emission properties for the complex fragment $[\text{Ni-NC}_{12}\text{H}_8]^+$ embedded in a symmetric $\kappa^3\text{-N,C,N}$ -bound 2,6-bis(pyrid-2-yl)phenyl framework.²³ Since orbital symmetry and ostensibly minor structural differences appear to have a pronounced impact on chromophore excited-state properties, we herein provide a detailed picture of the ground-state structure–property relationship for square-planar complex chromophores of Ni(II) in rigid, low-symmetry $\kappa^3\text{-N,N',C/O}$ -type environments. To this end, we have separately addressed the effects of (a) the *N*-heterocyclic moiety as charge acceptor for light-induced CT, (b) the fragment Ni–ER as the corresponding charge donor, and (c) C- versus O-metalation of the pendant aryl-linkage that connects the former two.

Effect of *N*-Heterocyclic Moiety. The electrochemical and visible absorption spectroscopic data corroborate that the *N*-heterocyclic backbone is electronically distinct from the pendant C-/O-aryl moiety even though their π -systems are coplanar. The role of a *N*-heterocycle borne π^* -orbital as the chromophore LUMO matches assignments for structurally related complexes of Ni²⁺^{21,39} and Pt²⁺^{29,40} and seminal work on the spin density distribution of radical anion complexes of

1,10-phenanthroline^{41,42} and dipyrido[3,2-*a*:2',3'-*c*]phenazine.^{43–45} The trend among the reduction potentials E_1^0 attests that extending the conjugation of the acceptor π -system provides the means to modulate the LUMO energy, albeit in a discontinuous fashion. Appending a pyrazine moiety to 1,10-phenanthroline **A** in the form of 10,11,12,13-tetrahydrodipyrido[3,2-*a*:2',3'-*c*]phenazine **B** has a marginal effect on the acceptor strength as the formal potential for the first reduction E_1^0 changes by +0.06 V. Contrary to the first reduction, extending the π -system has a marked effect on the second reduction that becomes electrochemically reversible. Such behavior points to an electronic compartmentalization of the π -orbital manifold such that first and second reduction locate at spatially different parts of *N*-heterocyclic fragment **B**, namely, at the κ^2 -*N,N'*-bipyridine and 10,11,12,13-tetrahydrophenazine moiety, respectively. In principle, this picture is reminiscent of the manifold of lowest unoccupied MOs of the parent ligand dipyrido[3,2-*a*:2',3'-*c*]phenazine in complexes of Ru(II) whose first and second reduction occur at spatially distinct π^* -type MOs but in reverse order, namely, at the phenazine and the bipyridine moiety, respectively.⁴³ Taking the π -conjugation one step further in the form of dipyrido[3,2-*a*:2',3'-*c*]phenazine **C** finally induces a substantial shift of E_1^0 (and E_2^0) to a more positive potential. Notably, the $\Delta E_1^0 \approx 0.3$ V is reminiscent to the change in reduction potentials reported for the (bipyridine)₂Ru(II) complex fragment of the respective κ^2 -*N,N'*-dipyrido[3,2-*a*:2',3'-*c*]phenazine parent ligands of **B** and **C**, albeit its electrochemical reduction is irreversible.⁴⁶ Rendering ligand reduction energetically more favorable however associates with a reduced capability for 3d- π^* -back-bonding and an increasing CT character for electronic transitions that connect to the LUMO. As a consequence, the respective absorption bands are expected to display a redshift and an increasingly negative solvatochromism. Inspection of the UV-vis-NIR absorption data indeed adds support to this picture in form of the high-energy visible band whose position shifts substantially to lower energy for ^CNi-SARTip₂ that exhibits the largest solvatochromism among ^{A/B/C}Ni-SARTip₂. This indicates a reversal of the order of unoccupied π^* -acceptor states in case of the C-type chromophores, namely, the phenazine fragment characterizes the LUMO, whereas the κ^2 -*N,N'*-bipyridine forms the LUMO+1. The computational analysis of unoccupied frontier MOs corroborates the picture of reversing acceptor state energies in the transition from **A** and **B** to C-type chromophores.

Observing very similar positions for the high-energy visible bands of pivaloato and carbazolido as well as for amido and thiolato complexes connects to their matching reduction potentials E_1^0 and supports the assignment of a HOMO-*n* (*n* ≥ 1)-to-LUMO CT character to the high-energy visible bands (400–500 nm region) for all chromophores ^{A/B/C}Ni-ER. Notably, a similar description was reported for transitions connecting to the LUMO of a structurally related chromophore of Pt(II) that derives from a C-type κ^3 -*N,N',C*-framework. The photoluminescence of the Pt(II) system was ascribed to a triplet excited-state of mixed intraligand π - π^* and MLCT parentage.⁴⁰ While the primary ligand framework suits to support photoluminescence as demonstrated by the Pt(II) congener, we attribute the dominant nonradiative decay of the Ni(II) chromophores to the combined effect of the CT character of the transition, the shallow potential well for rotational motion about the Ni-E bond and possible coordination of additional donors at nickel. In addition, energy

dissipation through energetically matched overtones of C-H stretching vibrations of the solvent and/or the ligand framework may be effective for excited-state quenching.⁴⁷ Light-promoted CT from the {Ni-ER} fragment into the π^* -manifold of the *N*-heterocycle results in a partial Ni(III) character of the electronic excited-state, which can further increase due to rotational motion about the Ni-E bond or the coordination of potential donors such as 2-Me-thf. The bonding of the (F₃CSO₂)₂N-anion inferred from EPR spectroscopic data adds support to the role of additional donors in excited-state quenching, and weak interactions between Ni and the ipso-C atom of the flanking 2,4,6-ⁱPr₃-phenyl groups may contribute in the case of the SARTip₂ coligand.⁴⁸ Finally, tetrahedral distortion at Ni can add a potential deactivation pathway toward an excited d-d state,^{25,26} even though this process may be regarded as unfavorable considering the overall rigidity of the primary ligand framework.

Effects of Coligand RE⁻. The combined effect of coligand RE⁻ and the *N*-heterocyclic backbone on chromophore ground-state electronic properties is the result of a fine balance of their respective π -donor and acceptor interactions with occupied d orbitals at nickel. Solid-state and solution structure analysis confirm that the lone-pair *np* orbital at E and the π^* orbitals at the κ^2 -*N,N'*-heterocyclic moiety adopt variable orientations. A perpendicular alignment prevails for ^ANi-NTMS₂²⁷ and presumably for ^CNi-NTMS₂, which renders *np*(E)- π^* (*N*-heterocycle)-orbital mixing through a Ni d orbital insignificant. The relative orbital alignment becomes more favorable in case of ^ANi-NC₁₂H₈, ^ANi-SARTip₂ and presumably ^CNi-OPh^tBu₂. In addition to relative spatial orientation, composition analysis of DFT-derived frontier orbitals indicates that the antibonding π -type Ni-E 3d-*np* orbital overlap becomes increasingly dominant along F₃CSO₂⁻ (see ref 27) \approx carboxylato < phenolato \approx carbazolido < amido < thiolato. The HOMO of ^ANi-OPiv carries only 12% ER character (>75% Ni), whereas the HOMO in ^ANi-SARTip₂ and ^ANi-NTMS₂ largely localize on ER with contributions of >50% each on the coordinated S and N atom (<20% Ni). In consequence, the antibonding π -type Ni-E 3d-*np* orbital overlap becomes increasingly dominant. Charge donation toward nickel increases accordingly and has a marked effect on the HOMO whose energy approaches that of the LUMO. The decreasing HOMO-LUMO energy gap relates to absorption profiles that increasingly expand across the visible spectral region. In more general terms, the capability of donor ligands to engage in π -type interactions with occupied metal d orbitals increases the manifold of chromophore donor states and aids absorptivity in the vis-NIR spectral region. Molar absorptivity scales with the degree of coplanar alignment of donor and acceptor orbitals and their mixing through an occupied metal d orbital. This aspect adds to the concept of extending the manifold of π -donor orbitals for symmetry allowed mixing with 3d orbitals in case of chromophores of octahedral Fe(II) and Fe(III).¹⁸

Independent support for the role of the antibonding 3d-2/3p π interaction on chromophore electronic properties derives from electrochemical and bulk oxidation studies. Potential values for the first oxidation are remarkably similar among the different donors for a given bonding mode κ^3 -*N,N',C/O*. As electrochemical oxidation is irreversible for nonamido donors, EPR data add vital information in form of the distinct anisotropy (and distribution) of the principal components of

the g and A tensors of oxidized amido and thiolato complexes $^A\text{Ni-ER}$ that corroborate the predominant contribution of E to the SOMO. Adopting a simplified picture, the order of the π -bond between the lone-pair $2/3p$ orbital at E and a doubly occupied $3d$ orbital is 0 and increases to $1/2$ upon oxidation, which is supported by the ligand-radical character inferred from EPR spectroscopic data in addition to the DFT-derived structure metrics that predict a contraction of the Ni-E bond by ≥ 0.1 Å upon oxidation; see Table S4. This description is independently supported by the visible absorption profile of the amidyl-radical complex cation formed from $^A\text{Ni-NTMS}_2$, namely, by the occurrence of an intense visible band at lower energy compared to the starting material and the persistence of the high-energy visible band whose intensity decreases. On the basis of these considerations, we attribute the low-energy visible bands to a HOMO-to-LUMO+ n ($n = 0$ and 1) type transition that involves CT from the π -type Ni-E $3d-np$ bond into a π^* -orbital at the $\kappa^2\text{-N,N'}$ -bipyridine fragment, namely, the LUMO in case of **A** and **B** and LUMO+1 for **C**. As described above, light-induced CT from the antibonding Ni-E $3d-np$ π -bond increases the Ni-E π -bond order to $1/2$ and thereby can contribute to kinetically disfavor the population of excited $d-d$ states that bear a metal-ligand antibonding character. A shallow potential well for Ni-E bond rotation however has a diametric effect and obviously plays a significant role as inferred from experimental and computational data.

Contrary to ligand-centered oxidation, metal-centered oxidation to Ni(III) associates with a reorganization of the coordination sphere through bonding of an additional donor. As indicated by a Mulliken spin density of $\rho_{\text{Ni}} = 0.88$ computed for $[\text{Ni-OPiv}]^+$, this scenario likely is relevant for nickel carboxylate complexes owing to the capability of carboxylates to κ^2 -bonding and provides an explanation for the irreversible character of their electrochemical oxidation. Unfortunately, the very low solubility of pivaloate complexes is incompatible with low-temperature solution studies to probe this scenario. The remarkable redox properties of the monodentate amido ligands for both C - and O -metalated chromophores line up with previous reports on pincer-type amidyl-radical complexes of Rh^{32} and Ni^{49} and a terminal amidyl-radical complex of Cu^{50} . The reversibility of the electrochemical oxidation points to a minor electronic and structure relaxation for the respective redox conjugates. We attribute the favorable electrode kinetics to polar effects that result from matching the nucleophilic character of the forming N -borne radical⁵¹ and the electrophilic character of the Ni(III) counterpart in preparation of the transition state. Contrary to amides as ligands, a polarity mismatch arises for the formation of O - and S -radicals that are electrophilic species the same as their Ni(III) counterpart and which is proposed to render the heterogeneous electron transfer step rate-limiting. Other than slow electrode kinetics, the pronounced lability of the $\text{Ni-thiyl-radical complex cation}$ compared with its amidyl congener is attributed to the more diffuse character of S $3p$ orbitals. The presence of a node in the radial function diminishes the overlap of a $3p$ orbital with the more compact (node-less) $3d$ orbital of Ni^{52} . More generally, the favorable kinetic stability of the unsupported $\text{Ni-amidyl fragment}$ is proposed to represent a key aspect that adds to the prominent role of the $3d$ -metal-amido fragment in designing luminescent base metal chromophore systems.^{23,28}

Effect of Pendant Aryl Moiety: C- versus O-Metalation. Substituting aryl for phenolate defines a setscrew for modulating chromophore frontier MO energies in a

fundamental fashion. While both donor systems are electronically distinct from the N -heterocycle π -system and therefore have a minor impact on LUMO energy, chromophore absorptivity in the low-energy visible region hinges on the choice of the pendant C -/ O -aryl side arm. Computational analysis indicates that both donors support σ - and π -bonding to Ni and contribute similarly to occupied frontier MOs for a given coligand RE^- but differ with regard to their impacts on orbital energies. In full agreement with electrochemical, absorption spectroscopic, and EPR data, the $\text{Ni-phenolate moiety}$ not only contributes substantially to the HOMO of $^A\text{-O-Ni-NTMS}_2$ but also renders the HOMO energetically more stable compared to that of C -metalated $^A\text{Ni-NTMS}_2$. While the LUMO energies appear largely conserved, an energetically stabilized HOMO and destabilized LUMO+ n ($n \geq 2$) prevail for O -metalated chromophore systems, in line with the lack of low-energy bands in the vis-region.

CONCLUSIONS

Structurally dissymmetric complexes of the general formula $[(\kappa^3\text{-N,N',C/O})\text{Ni-ER}]$ provide a platform toward electronically variable complex chromophores of planar Ni(II) . π -Bonding of an occupied Ni $3d$ orbital with an np electron pair at coligand RE^- provides a mechanism for coupling the latter to the π^* orbital manifold at the N -heterocyclic moiety for light-induced charge transfer, which results in substantial chromophore absorptivity across the visible spectral region. Molar absorptivity scales with the relative alignment of donor and acceptor orbitals and maximizes for a coplanar orientation. Frontier molecular orbital compositions and relative energies can be modulated by considering three principal factors. The first is the π -orbital manifold at the $\kappa^2\text{-N,N'}$ -coordinate N -heterocyclic moiety whose electronic coupling to Ni(II) through $d-\pi^*$ back-bonding has an impact on the character of the electronic excitation. Second, the pendant C -/ O -aryl fragment sets the energies of occupied donor and unoccupied acceptor frontier MOs other than the LUMO. Third, the σ - and π -donor capability of coligand RE^- controls transition energies and electronic relaxation upon light-induced electron transfer from the Ni-ER fragment.

Understanding the balance of the three contributions leads us to conclude that rotational motion about the Ni-E bond admixes Ni(III) character to the electronically excited state populated by $\{\text{Ni-ER}\}$ -to- $\{N\text{-heterocycle}-\pi^*\}$ charge transfer and thereby promotes predominant nonradiative decay of excited-state energy for this particular class of chromophores of square-planar Ni(II) . Further studies in glass matrices of deuterated solvents are underway to address additional contributions to excited-state quenching such as through solvent coordination and coupling to overtones of high-energy $C-H$ stretching vibrations. As to intramolecular contributions, future directions include setting coplanar geometric alignment of the Ni-ER $3d-np$ π -bond with respect to the manifold of π^* orbitals at the N -heterocycle fragment.

EXPERIMENTAL SECTION

Manipulations of air- and moisture-sensitive compounds were carried out under an atmosphere of dry argon using standard Schlenk or glovebox techniques. Information on the purification of reagents and solvents, and preparation of new proligands $^B/C\text{-O-OPiv}$ is provided in the Supporting Information. The following reagents and starting materials were prepared according to reported procedures: $1,1'$ -Bis(acetyl)ferrocenium bis(trifluoromethanesulfonyl)imide,⁵³ $[\text{Fc}''^-]$ -

NTf₂, tris(4-bromophenyl)ammonium tetrakis(3,5-bis(trifluoromethyl)phenyl)borate,⁵⁴ [(4-BrC₆H₄)₃N]BAr^F₄, 5-*tert*-butyl-2-methoxyphenyllithium,^{2,7} NaN(SiMe₃)₂,⁵⁵ KC₇H₇,^{5,6} 2,6-(2,4,6-Pr₃C₆H₂)₂C₆H₃SH,⁵⁷ Tip₂ArSH, ^ANi-OPiv, ^{A-O}Ni-NTMS₂, and [(^{A-O}Ni-thf)₂(μ-Tf)]OTf²⁷ [Tf = κ-O,O'-F₃CSO₂⁻, OTf = F₃CSO₃⁻].

Preparation of ^ANi-NC₁₂H₈. A toluene suspension of carbazole (23 mg, 0.138 mmol) and red KC₇H₇ (18 mg, 0.14 mmol) was stirred until only pale yellow KNC₁₂H₈ was observed. Toluene was removed under vacuum, and ^ANi-OPiv (65 mg, 0.14 mmol) was added. The solids were dissolved in 1,2-difluorobenzene (15 mL) to give a dark yellow mixture that was stirred for 2 h. A dark yellow solution was separated from KOPIV by cannula filtration and dried under vacuum to afford an ochre solid. The solid was extracted with toluene (total of 35 mL), and the extract solutions were filtered. The combined solutions were concentrated to ~5 mL and stored at 5 °C overnight. Dark yellow crystals were deposited, separated, washed with pentane, and finally dried under vacuum. Yield: 46 mg (0.09 mmol, 62%). Elemental analysis calcd. (%) for C₃₄H₂₇N₃Ni: C, 76.15; H, 5.07; N, 7.84. Found: C, 75.97; H, 5.08; N, 7.81. Unit cell parameters: *a* = 12.5383(4), *b* = 17.1643(5), *c* = 19.9812(6) Å; α = 66.877(2), β = 78.741(2), γ = 87.577(2)°; *V* = 3875.8(2) Å³, *Z* = 4, *P1*. Deposition number CCDC 2060410. UV-vis (THF, 24 °C): λ (ε/10³/M⁻¹ cm⁻¹) = 277 (58.7), 300 (28.8), 311 (27.6), 349 (16.4; shoulder), 364 (21.6), 385 (8.9; shoulder), 429 (7.8), 486 (3.8), 616 (1.0) nm. ¹H NMR (600 MHz, C₆D₆, 25 °C): δ = 8.59 (m, 4H, H25/28/31/34), 7.62 (ddd, *J* = 1.0, 6.9, 8.0, 2H, H27/33), 7.43 (ddd, *J* = 1.0, 6.9, 8.0, 2H, H26/32), 7.41 (d, *J* = 2.2, 1H, H3), 7.23 (d, *J* = 8.6, 1H, H10), 7.18 (dd, *J* = 1.2, 4.9, 1H, H16), 6.98 (d, *J* = 8.5, 1H, H11), 6.90 (dd, *J* = 1.2, 8.1, 1H, H14), 6.86 (d, *J* = 8.8, 1H, H17), 6.68 (d, *J* = 8.8, 1H, H18), 6.56 (dd, *J* = 2.2, 8.1, 1H, H5), 6.50 (d, *J* = 8.1, 1H, H6), 5.99 (dd, *J* = 4.9, 8.1, 1H, H15), 1.23 (s, 9H, H20/21/22) ppm. ¹³C NMR (151 MHz, C₆D₆, 25 °C): δ = 164.3 (C7), 151.1 (2C, C23/29), 150.5 (C16), 149.7 (C1), 148.4 (C4), 147.9 (C2), 146.4 (C12), 146.3 (C8), 141.1 (C6), 136.1 (C14), 135.7 (C10), 129.6 (C5), 128.7 (C13; masked by solvent), 127.7 (2C, C24/30), 125.8 (C15), 125.7 (C9), 125.6 (C17), 124.6 (2C, C27/33), 124.5 (C18), 120.8 (2C, C28/34 or C25/31), 120.1 (C3), 118.0 (C11), 116.3 (2C, C26/32), 116.3 (2C, C25/31 or C28/34), 34.7 (C19), 31.8 (3C, C20–22) ppm.

Preparation of ^ANi-SARTip₂. Addition of OEt₂ (10 mL) to a mixture of colorless Tip₂ArSK, obtained from Tip₂ArSH (55 mg, 0.106 mmol) and KC₇H₈ (14 mg, 0.11 mmol) in toluene (2 g), and brick-red ^ANi-OPiv (50 mg, 0.11 mmol) afforded a dark green solution immediately upon stirring. The solvent was removed under vacuum after stirring for 2.5 h. The residual green solid was extracted successively with toluene, and the green extracts were filtered. No crystallization was observed from either toluene or pentane but from OEt₂ (5 mL) within 7 days at -28 °C. Dark green microcrystals were separated from a pale green supernatant by cannula filtration and dried under vacuum. Yield: 55 mg (0.06 mmol, 59%). Single crystals for XRD structure analysis were obtained from a C₆D₆ solution through slow layer diffusion of (Me₃Si)₂O at room temperature, affording dark green ^ANi-SARTip₂ × 0.5C₆D₆. Elemental analysis calcd. (%) for C₅₈H₆₈N₂NiS: C, 78.81; H, 7.75; N, 3.17; S, 3.63. Found: C, 78.83; H, 7.43; N, 3.17; S, 3.08. Unit cell parameters: *a* = 34.9672(11), *b* = 15.9198(5), *c* = 19.7110(6) Å; α = 90, β = 112.474(2), γ = 90°; *V* = 10139.2(6) Å³, *Z* = 8, *C2/c*. Deposition number CCDC 2060409. UV-vis (THF, 24 °C): λ (ε/10³/M⁻¹ cm⁻¹) = 306 (26.2), 314 (25.0; shoulder), 327 (19.8; shoulder), 368 (10.3; shoulder), 455 (6.5), 606 (3.3; shoulder), 636 (3.4) nm. 1,2-C₆H₄F₂ (22 °C): λ (ε/10³/M⁻¹ cm⁻¹) = 310 (22.7), 366 (9.8; shoulder), 454 (5.7), 589 (3.1; shoulder), 632 (3.5) nm. ¹H NMR (600 MHz, C₆D₆, 25 °C): δ = 8.19 (dd, *J* = 1.3, 5.0, 1H, H16), 7.45 (d, *J* = 7.7, 2H, H25/27), 7.34 (d, *J* = 8.0, 1H, H6), 7.27 (d, *J* = 2.4, 1H, H3), 7.25 (t, *J* = 7.6, 1H, H26), 7.20 (br s, 4H, H31/33/37/39), 7.19 (dd, *J* = 1.5, 8.3, 1H, H14), 7.14 (d, *J* = 8.5, 1H, H10), 7.04 (dd, *J* = 2.2, 8.0, 1H, H5), 6.92 (d, *J* = 8.5, 1H, H11), 6.77 (m, 2H, H17/18), 6.54 (dd, *J* = 5.0, 8.1, 1H, H15), 3.48 (sep, *J* = 6.8, 4H, H41/43/44/46), 2.68 (sep, *J* = 6.9, 2H, H42/45), 1.43 (br s, 12H, H47/48/

51/52), 1.37 (br d, *J* = 6.8, 12H, H53/54/57/58), 1.34 (s, 9H, H20/21/22), 1.02 (d, *J* = 6.8, 12H, H49/50/55/56) ppm. ¹³C NMR (151 MHz, C₆D₆, 25 °C): δ = 160.4 (C7), 147.8 (C2), 147.7 (C23), 147.6 (C16), 147.6 (2C, C24/28), 147.6 (C1), 147.6 (4C, C30/34/36/40), 147.4 (C4), 147.4 (2C, C32/38), 145.7 (C12), 144.1 (C8), 141.5 (C6), 141.1 (2C, C29/35), 137.0 (C14), 134.5 (C10), 131.2 (2C, C25/27), 128.4 (C13; masked by solvent), 127.4 (C5), 126.0 (C17), 125.7 (C9), 125.5 (C18), 124.1 (C15), 123.4 (C26), 121.2 (br, 4C, C31/33/37/39), 119.2 (C3), 117.4 (C11), 34.9 (C42/45), 34.7 (C19), 32.0 (3C, C20–22), 31.7 (4C, C41/43/44/46), 26.9 (4C, C47/48/51/52 or C53/54/57/58), 24.6 (4C, C49/50/55/56), 24.5 (4C, C53/54/57/58 or C47/48/51/52) ppm.

Preparation of ^{A-O}Ni-SARTip₂. Addition of OEt₂ (10 mL) to a mixture of colorless Tip₂ArSK, obtained as a solid from Tip₂ArSH (97 mg, 0.19 mmol) and KC₇H₈ (25 mg, 0.19 mmol) in toluene (2 g) solution, and pale green [(^{A-O}Ni-thf)₂(μ-Tf)]OTf (110 mg, 0.19 mmol) afforded a dark red solution within a few minutes of stirring. The solution was filtered after stirring for 1 h. The residual solid was extracted with OEt₂ (2 × 10 mL) until no more red product could be removed, and the solvent was removed under vacuum. Dissolution of the residual dark red solid in pentane (10 mL) afforded a dark red solution from which crystals separated upon reducing the volume (3 mL) and cooling at -28 °C overnight. A pale red supernatant was removed by cannula filtration, and the crystalline product was dried under vacuum. Yield: 140 mg (0.16 mmol, 82%) of dark red microcrystalline ^{A-O}Ni-SARTip₂. The microcrystals were dissolved in C₆H₆ (~1 mL) and crystallized through layer diffusion of (Me₃Si)₂O, which deposited dark red prisms of ^{A-O}Ni-SARTip₂ × 0.5C₆H₆. Crystals for XRD analysis were grown from layer diffusion of (Me₃Si)₂O into a dark red solution in CDCl₃. Elemental analysis calcd. (%) for C₅₈H₆₈N₂NiOS × 0.5C₆H₆: C, 78.03; H, 7.62; N, 2.98; S, 3.41. Found: C, 77.99; H, 7.33; N, 3.01; S, 2.82. Unit cell parameters: *a* = 37.0050(7), *b* = 37.0050(7), *c* = 14.5311(3) Å; α = β = γ = 90°; *V* = 19898.5(9) Å³, *Z* = 16, *I41/a*. Deposition number CCDC 2060408. UV-vis (THF, 24 °C): λ (ε/10³/M⁻¹ cm⁻¹) = 267 (39.8; shoulder), 287 (28.9; shoulder), 306 (28.2), 319 (22; shoulder), 376 (26), 479 (9.4), 522 (7.0; shoulder), 699 (0.2) nm. ¹H NMR (600 MHz, CDCl₃, 25 °C): δ = 8.31 (dd, *J* = 1.2, 5.4, 1H, H16), 8.22 (d, *J* = 9.2, 1H, H11), 8.07 (d, *J* = 8.9, 1H, H10), 7.99 (dd, *J* = 1.2, 8.1, 1H, H14), 7.71 (d, *J* = 2.4, 1H, H3), 7.48 (d, *J* = 8.6, 1H, H17), 7.42 (d, *J* = 8.6, 1H, H18), 7.35 (t, *J* = 7.6, 1H, H26), 7.17 (d, *J* = 7.5, 2H, H25/27), 7.12 (dd, *J* = 2.4, 8.9, 1H, H5), 7.00 (br s, 4H, H31/33/37/39), 6.93 (dd, *J* = 5.4, 8.1, 1H, H15), 6.17 (d, *J* = 8.9, 1H, H6), 3.03 (br s, *v*_{1/2} ~ 60 Hz, 4H, H41/43/44/46), 2.73 (sep, *J* = 6.9, 2H, H42/45), 1.35 (s, 9H, H20/21/22), 1.02 (d, *J* = 7.1, 12H, H48/51), 1.35 and 1.01 (br s each, 24H, H47/49/50/52) ppm. ¹³C NMR (151 MHz, CDCl₃, 25 °C): δ = 161.9 (C1), 151.1 (C7), 150.4 (C16), 146.9 (2C, C24/28), 146.7 (4C, C30/34/36/40), 146.2 (2C, C32/38), 144.3 (C23), 143.1 (C12), 143.0 (C8), 140.3 (2C, C29/35), 136.8 (C4/14), 133.9 (C10), 129.6 (C5), 129.5 (2C, C25/27), 127.1 (C13), 125.6 (C18), 125.0 (C9), 124.7 (C17), 124.0 (C6), 122.9 (C26), 122.2 (C15), 121.4 (C11), 121.3 (C3), 120.2 (br, *v*_{1/2} = 48 Hz, 4C, C31/33/37/39), 117.0 (C2), 34.0 (2C, C42/45), 34.0 (C19), 31.5 (3C, C20–22), 30.4 (br, *v*_{1/2} = 60 Hz, 4C, C41/43/44/46), 25.7 and 23.4 (br, 4C, C47/49/50/52), 24.0 (2C, C48/51) ppm.

Preparation of ^BNi-OPiv. A suspension of proligand ^BO-OPiv (90 mg, 0.17 mmol) in toluene (2.5 g) was transferred by pipet to a toluene solution (2.5 g) of Ni(cod)₂ (48 mg, 0.17 mmol) in the glovebox, affording a dark green solution. Separation of a brown-red crystalline precipitate was noted within 1 h at room temperature, and stirring was continued for another 16 h after which the supernatant was removed by cannula filtration, the residual crystalline mass washed twice with pentane and dried under dynamic vacuum. Yield: 81 mg (0.14 mmol, 81%) of ^BNi-OPiv × 0.5C₇H₈ as reddish-brown, hairlike crystals. Elemental analysis calcd (%) for C₃₃H₃₄N₄NiO₂ × 0.5C₇H₈: C, 70.32; H, 6.14; N, 8.99. Found: C, 69.55; H, 6.24; N, 9.10. Unit cell parameters: *a* = 8.2710(6), *b* = 12.0751(8), *c* = 15.0435(11) Å; α = 83.787(4), β = 83.284(4), γ = 86.569(4)°; *V* = 1481.67(18) Å³, *Z* = 1, *P1*. Deposition number CCDC 2060407. UV-vis (THF, 28 °C): λ (ε/10³/M⁻¹ cm⁻¹) = 326 (27.3), 350 and

365 (25.5), 431 (7.7), 446 (6.8; shoulder), 513 (3.1), 554 (1.2; shoulder) nm. IR (KBr, transmission): $\bar{\nu}$ = 1612 (carbonyl stretch) cm^{-1} .

Preparation of $^{\text{B}}\text{Ni-SArTip}_2$. $^{\text{B}}\text{Ni-OPiv}$ ($\times 0.5\text{C}_7\text{H}_8$ (60 mg, 96 μmol) was added to colorless solid KSArTip_2 that was prepared from HSArTip_2 (53 mg, 100 μmol) and KC_7H_8 (14 mg, 100 μmol) in toluene (2 g) solution. Addition of OEt_2 (10 mL) to the solids affords a dark green solution within few minutes of stirring. The solution was filtered and the residual solids were extracted with OEt_2 (2×10 mL) until no more green product could be removed. The volume of the combined OEt_2 solution was reduced until crystallization occurred, and the mixture was stored at -30 $^{\circ}\text{C}$ overnight. The supernatant was removed at -30 $^{\circ}\text{C}$, and the residual dark green crystalline solid was dried under dynamic vacuum. Yield: 66 mg (67 μmol , 70%) dark green crystalline solid. Elemental analysis calcd (%) for $\text{C}_{64}\text{H}_{74}\text{N}_4\text{NiS}$: C, 77.64; H, 7.53; N, 5.66; S, 3.24. Found: C, 77.64; H, 7.17; N, 5.64; S, 3.09. ^1H NMR (600 MHz, C_6D_6): δ = 9.22 (d, J = 8.1, 1H, H16), 8.51 (dd, J = 1.1, 5.2, 1H, H14), 8.41 (d, J = 8.3, 1H, H10), 7.51 (d, J = 7.7, 2H, H31/33), 7.43 (d, J = 8.0, 1H, H6), 7.35 (br s, 4H, H37/39/43/45), 7.33 (t, J = 7.7, 1H, H32), 7.13 (d, J = 2.0, 1H, H3), 7.10 (dd, J = 7.9, 5.1, 1H, H15), 7.03 (dd, J = 2.2, 8.1, 1H, H5), 6.65 (d, J = 8.5, 1H, H11), 3.62 (br sep, 4H, H47/48/50/51), 2.88 (m, 2H, H25/26/27/28), 2.79 (br sep, 2H, H49/52), 2.55 (m, 2H, H25/26/27/28), 1.55 (m, 4H, H25/26/27/28), 2.34–0.64 (very br s, 12H, H53–56, H59–62), 1.48 (br s, 12H, H53–56, H59–62), 1.31 (s, 9H, H22/23/24), 1.14 (br d, 12H, H57/58/63/64) ppm. ^{13}C NMR (151 MHz, C_6D_6): δ = 160.9 (C7), 153.6 and 153.5 (C19/21), 149 (2C, C30/34), 147.9 (C14), 147.7 (4C, C36/40/42/46), 147.6 (3C, C1 and C38/44), 147.3 (C4), 147.2 (C2), 146.6 (2C, C35/41), 146.5 (C18), 144.9 (C17), 141.8 (C6), 141.0 (C29), 137.2 (C12), 137.1 (C8), 136.3 (C16), 131.4 (2C, C31/33), 130.4 (C10), 128.8 (C15), 127.6 (C5), 127.1 (C13), 124.5 (C32), 123.3 (C9), 121.5 (4C, C37/39/43/45), 119 (C3), 116.2 (C11), 35.0 (2C, C49/52), 34.7 (C21), 33.4 (C25), 32.4 (C26), 31.9 (3C, C22–24), 31.8 (4C, C47/48/50/51), 26.8 and 25.0 (8C, C53–56, C59–62), 24.8 (4C, C57/58/63/64), 23.4 and 23.2 (2C, C25/28) ppm. UV–vis (THF, 25 $^{\circ}\text{C}$): λ ($\epsilon/10^3/\text{M}^{-1}\text{cm}^{-1}$) = 282 (57.6), 301 (44; shoulder), 327 (39.8; shoulder), 350 (35; shoulder), 371 (23.9; shoulder), 458 (11.1), 524 (4.4; shoulder), 623 (4.5; shoulder), 648 (4.6) nm. $^{1,2}\text{-C}_6\text{H}_4\text{F}_2$ (22 $^{\circ}\text{C}$): λ ($\epsilon/10^3/\text{M}^{-1}\text{cm}^{-1}$) = 288 (44.1; shoulder), 328 (34.5), 346 (29.5), 372 (18.5; shoulder), 454 (9.3), 589 (4.0; shoulder), 637 (4.6) nm.

Preparation of $^{\text{C}}\text{Ni-OPiv}$. The procedure is analogous to that described above for $^{\text{B}}\text{Ni-OPiv}$, except for the following changes: $^{\text{C}}\text{O-OPiv}$, 120 mg (0.19 mmol); $\text{Ni}(\text{cod})_2$, 52 mg (0.19 mmol), toluene (6.2 g). Yield: 113 mg (0.16 mmol, 86%) of hairlike ochre crystals. Elemental analysis calcd (%) for $\text{C}_{42}\text{H}_{46}\text{N}_4\text{NiO}_2$: C, 72.32; H, 6.65; N, 8.03. Found: C, 71.94; H, 6.70; N, 8.03. UV–vis (THF, 28 $^{\circ}\text{C}$): λ ($\epsilon/10^3/\text{M}^{-1}\text{cm}^{-1}$) = 295 (61.5), 310 (45.5; shoulder), 375 (48.7), 385 (42.4; shoulder), 468 (9.5), 510 (6.5; shoulder), 560 (2.2; shoulder) nm. IR (KBr, transmission): $\bar{\nu}$ = 1612 (carbonyl stretch) cm^{-1} .

Preparation of $^{\text{C}}\text{Ni-OPh}^t\text{Bu}_2$. $^{\text{C}}\text{Ni-OPiv}$, prepared as described above from $^{\text{C}}\text{O-OPiv}$ (50 mg; 78 μmol) and $\text{Ni}(\text{cod})_2$ (22 mg; 79 μmol), was combined with KOPh^tBu_2 , prepared from 2,4-di-*tert*-butylphenol (16 mg, 78 μmol) and KC_7H_7 (10 mg, 78 μmol) in toluene (7 g), in 1,2-difluorobenzene (10 mL) to afford a dark red solution within a few minutes of stirring. Solvent was removed after 1 h. The residual solid was washed with pentane (40 mL), dissolved in 1,2-difluorobenzene, and crystallized by slow layer diffusion of $(\text{Me}_3\text{Si})_2\text{O}$. Reddish hairlike crystals separated within days and were separated by cannula filtration, washed with pentane, and dried under vacuum. Yield: 24 mg (30 μmol , 38%). Elemental analysis calcd (%) for $\text{C}_{51}\text{H}_{58}\text{N}_4\text{NiO}$: C, 76.40; H, 7.29; N, 6.99. Found: C, 74.22; H, 7.24; N, 6.86. ^1H NMR (600 MHz, C_6D_6 , 25 $^{\circ}\text{C}$): δ = 9.04 (d, J = 8.4, 1H, H10), 8.91 (dd, J = 1.3, 8.0, 1H, H14), 8.45 (d, J = 8.2, 1H, H39), 8.34 (dd, J = 1.5, 5.0, 1H, H16), 8.26 (s, 1H, H21), 8.14 (s, 1H, H24), 7.76 (d, J = 2.6, 1H, H42), 7.47 (d, J = 8.0, 1H, H6), 7.46 (d, J = 2.0, 1H, H3), 7.45 (dd, J = 2.5, 8.5, 1H, H40), 7.08 (d, J = 8.5, 1H, H11), 6.97 (dd, J = 2.1, 8.0, 1H, H5), 6.61 (dd, J = 4.9, 8.2, 1H,

H15), 2.16 (s, 9H, H46/47/48), 1.53 (s, 9H, H49/50/51), 1.33 (s, 9H, H35/36/37), 1.26 (s, 6H, H29/30), 1.25 (s, 6H, H33/34), 0.77 (s, 6H, H31/32). ^{13}C NMR (151 MHz, C_6D_6 , 25 $^{\circ}\text{C}$): δ = 165.8 (C38), 165.1 (C7), 158.3 (C22), 157.8 (C23), 150.7 (2C, C16/18), 150.2 (C1), 148.3 (2C, C4/17), 147.6 (C12), 146.7 (C2), 143.5 (C20), 142.8 (C19), 140.1 (C8), 139.6 (C41), 139.4 (C6), 136.0 (C43), 134.0 (C14), 132.6 (C10), 128.4 (C13; masked by solvent), 129.3 (C5), 126.3 (C15), 125.0 (C9), 124.5 (C39), 124.3 (C40), 123.3 (C21), 123.1 (2C, C24/42), 119.9 (C3), 118.3 (C11), 49.5 (C26), 48.7 (C27), 48.6 (C25), 36.7 (C45), 35.0 (C28), 34.9 (C44), 33.0 (3C, C49–51), 32.1 (3C, C35–37), 31.1 (3C, C46–48), 28.5 (2C, C33/34), 28.4 (2C, C29/30), 22.0 and 21.9 (2C, C31/32). UV–vis (THF, 26 $^{\circ}\text{C}$): λ ($\epsilon/10^3/\text{M}^{-1}\text{cm}^{-1}$) = 297 (62), 310 (49; shoulder), 376 (50), 385 (46.5; shoulder), 472 (10.5), 513 (7.2; shoulder), 606 (2.0; shoulder) nm.

Preparation of $^{\text{C}}\text{Ni-SArTip}_2$. Addition of OEt_2 (15 mL) to a mixture of colorless Tip_2ArSK , obtained from Tip_2ArSH (44 mg, 86 μmol) and KC_7H_8 (11 mg, 86 μmol) in toluene (4 g), and ochre $^{\text{A}}\text{Ni-OPiv}$ (60 mg, 86 μmol) afforded a red-purple solution upon stirring for 0.5 h. The solvent was removed under vacuum after stirring for 5 h. The residual dark red solid was extracted successively with OEt_2 , and the red-purple extracts were filtered, combined, and dried under vacuum. The residual solid was dissolved in $(\text{Me}_3\text{Si})_2\text{O}$ (10 mL), and the volume was slowly reduced to ~ 5 mL, leading to the separation of dark red crystals. Crystallization was completed at 4 $^{\circ}\text{C}$ overnight; dark red microcrystals were separated from a pale purple supernatant by cannula filtration and dried under vacuum. Yield: 68 mg (58 μmol , 68%) of purple $^{\text{C}}\text{Ni-SArTip}_2 \times 1/3(\text{Me}_3\text{Si})_2\text{O}$. Dark red single crystals for XRD analysis were separated from a $\text{C}_6\text{D}_6/(\text{Me}_3\text{Si})_2\text{O}$ (0.5/3 mL) solution kept at -35 $^{\circ}\text{C}$ for 3 months. Elemental analysis calcd (%) for $\text{C}_{73}\text{H}_{86}\text{N}_4\text{NiS} \times 1/3\text{C}_6\text{H}_8\text{OSi}_2$: C, 77.36; H, 7.96; N, 4.81; S, 2.75. Found: C, 77.35; H, 7.59; N, 4.81; S, 2.63. Unit cell parameters: a = 14.7177(6), b = 19.1313(8), c = 31.7880(14) \AA ; α = 99.367(2), β = 101.410(2), γ = 93.719(2) $^{\circ}$; V = 8612.92 \AA^3 , Z = 4, $P1$. ^1H NMR (600 MHz, C_6D_6 , 25 $^{\circ}\text{C}$): δ = 9.10 (dd, J = 1.3, 8.0, 1H, H16), 8.76 (dd, J = 1.1, 5.0, 1H, H14), 8.67 (d, J = 8.3, 1H, H10), 8.15 (s, 1H, H25), 8.03 (s, 1H, H28), 7.49 (d, J = 7.6, 2H, H40/42), 7.36 (d, J = 8.0, 1H, H6), 7.30 (br s, 4H, H46/48/52/54), 7.30 (t, J = 7.6, 1H, H41), 7.26 (d, J = 2.1, 1H, H3), 7.05 (dd, J = 2.2, 8.2, 1H, H5), 6.97 (m, 2H, H11 and H15), 3.58 (sep, J = 6.7, 4H, H56/58/59/61), 2.74 (sep, J = 6.8, 2H, H57/60), 1.57 (br s, $\nu_{1/2}$ = 55 Hz, 12H, H68/69/72/73), 1.42 (br d, J = 7.0, 12H, H62/63/66/67), 1.29 (s, 9H, H20/21/22), 1.28 (s, 6H, H32/33), 1.23 (s, 6H, H36/37), 1.10 (d, J = 6.8, 12H, H64/65/70/71), 0.78 (s, 6H, H35/35), 0.12 (s, 6H, $1/3(\text{Me}_3\text{Si})_2\text{O}$) ppm. ^{13}C NMR (151 MHz, C_6D_6 , 25 $^{\circ}\text{C}$): δ = 162.5 (C7), 157.7 (C27), 157.2 (C26), 149.7 (C14), 148.5 (C12), 148.4 (2C, C39/43), 147.8 (C1), 147.7 (4C, C45/49/51/55), 147.5 (4C, C2/4/47/53), 147.4 (C38), 147.1 (C8), 143.2 (C23), 142.8 (C24), 141.6 (C6), 141.0 (2C, C44/50), 139.7 (2C, C17/18), 134.7 (C16), 131.4 (2C, C40/42), 131.1 (C10), 128.2 (C13; masked by solvent), 127.6 (C5), 127.1 (C15), 124.3 (C9), 123.9 (C41), 123.1 (C28), 122.9 (C25), 121.3 (4C, C46/48/52/54), 119.3 (C3), 117.6 (C11), 49.4 (C30), 48.4 (2C, C29/31), 34.9 (2C, C57/60), 34.6 (C19), 31.9 (3C, C20–22), 31.8 (4C, C56/58/59/61), 28.5 (2C, C32/33), 28.3 (2C, C36/37), 26.8 (4C, C62/63/66/67), 24.8 (4C, C68/69/72/73), 24.7 (4C, C64/65/70/71), 21.9 (2C, C35/35), 2.41 ($1/3(\text{Me}_3\text{Si})_2\text{O}$) ppm. UV–vis (THF, 24 $^{\circ}\text{C}$): λ ($\epsilon/10^3/\text{M}^{-1}\text{cm}^{-1}$) = 299 (70.1), 317 (57.1; shoulder), 380 (44.2; shoulder), 394 (51.4), 447 (7.6; shoulder), 500 (9.2), 654 (4.1) nm. $^{1,2}\text{-C}_6\text{H}_4\text{F}_2$ (24 $^{\circ}\text{C}$): λ ($\epsilon/10^3/\text{M}^{-1}\text{cm}^{-1}$) = 302 (56.7), 323 (42.5), 380 (39.7), 394 (39.7), 448 (6.1), 488 (7.1), 645 (4.0) nm. *n*-pentane (24 $^{\circ}\text{C}$): λ ($\epsilon/10^3/\text{M}^{-1}\text{cm}^{-1}$) = 236 (77.8), 280 (66.7), 291 (71.7), 303 (67.4), 380 (43.4), 396 (44.5), 451 (6.5), 512 (8.9), 677 (3.3) nm.

Preparation of $^{\text{C}}\text{Ni-NTMS}_2$. To a suspension of $^{\text{C}}\text{Ni-OPiv}$ in toluene (10 g), prepared as described above from $^{\text{C}}\text{O-OPiv}$ (75 mg; 0.12 mmol) and $\text{Ni}(\text{cod})_2$ (33 mg; 0.12 mmol), was added NaNNTMS_2 (22 mg, 0.12 mmol) dissolved in thf (8 g). After stirring for 3 h, solvents were removed under vacuum, and the solid residue washed with pentane (50 mL), extracted with hexanes (3×75 mL). The extracts were filtered, combined, concentrated until a crystalline solid

separated, and stored at $-40\text{ }^{\circ}\text{C}$ to deposit brick red microcrystals. The supernatant was removed by cannula filtration, and the microcrystalline product was dried under vacuum. Yield: 10 mg (0.01 mmol, 11%). ^1H NMR (600 MHz, C_6D_6 , $25\text{ }^{\circ}\text{C}$): δ = 9.12 (d, J = 7.6, 1H, H14), 9.05 (dd, J = 1.2, 4.9, 1H, H16), 9.02 (d, J = 8.3, 1H, H10), 8.24 (s, 1H, H21), 8.21 (s, 1H, H24), 8.10 (d, J = 7.9, 1H, H6), 7.49 (d, J = 1.8, 1H, H3), 7.47 (dd, J = 2.2, 8.1, 1H, H5), 7.18 (d, J = 8.7, 1H, H11), 6.97 (dd, J = 4.7, 8.1, 1H, H15), 1.38 (s, 9H, H35/36/37), 1.25 (s, 6H, H29/30), 1.24 (s, 6H, H33/34), 0.85 (s, $J_{\text{H-Si}}$ = 6.1, 18H, $(\text{Me}_3\text{Si})_2\text{N}$), 0.75 (s, 6H, H31/32). ^{13}C NMR (151 MHz, C_6D_6 , $25\text{ }^{\circ}\text{C}$): δ = 165.5 (C7), 158.2 (C22), 157.8 (C23), 151.2 (C16), 148.5 (C8 or C12), 148.4 (C12 or C8), 148.3 (C1), 148.0 (C4), 147.5 (C2), 143.5 (C20), 142.9 (2C, C6/19), 140.5 (C17), 139.9 (C18), 134.5 (C14), 132.5 (C10), 128.4 (2C, C5/13; masked by solvent), 126.2 (C15), 125.3 (C9), 123.2 (C24), 123.1 (C21), 120.3 (C3), 118.4 (C11), 49.5 (C26), 48.7 (C25 or C27), 48.6 (C27 or C25), 35.0 (C28), 32.1 (3C, C35–37), 28.5 (2C, C29 or C30, C33 or C34), 28.4 (2C, C30 or C29, C34 or C33), 22.0 (2C, C31/32), 7.81 (6C, J = 53.6, $(\text{Me}_3\text{Si})_2\text{N}$). UV–vis (THF, $24\text{ }^{\circ}\text{C}$): λ ($\epsilon/10^3/\text{M}^{-1}\text{ cm}^{-1}$) = 292 (89.2), 315 (67.1; shoulder), 358 (46.1; shoulder), 379 (67.1), 389 (68.5), 492 (12.6), 543 (9.0; shoulder) nm.

In situ Oxidation of $^{\text{A}}\text{Ni-NTMS}_2$. To a red solution of $^{\text{A}}\text{Ni-NTMS}_2$ (2 mg, $4\text{ }\mu\text{mol}$) in toluene (1.74 g) in a 25 mL septum capped Schlenk flask cooled at $-78\text{ }^{\circ}\text{C}$ (acetone/dry ice) was added a blue solution of $[(4\text{-BrC}_6\text{H}_4)_3\text{N}]\text{BAR}^{\text{F}_4}$ (5 mg, $4\text{ }\mu\text{mol}$) at $\leq -40\text{ }^{\circ}\text{C}$ in CH_2Cl_2 (2.0 mL; in Ar supplied 4 mL screw cap vial with septum) to afford an emerald green solution instantaneously upon mixing. A $\sim 0.3\text{ mL}$ portion of this solution was transferred through a precooled double-tipped cannula into a septum-capped EPR sample tube at $-78\text{ }^{\circ}\text{C}$ and was immediately frozen at 77 K for X-band cw-EPR characterization. Figures S6 and S7 provide details for spectra recorded at 100 and 213 K, respectively. Simulation parameters, 100 K: $g_{x,y,z}$ = 2.110, 2.068, and 2.0279; $g\text{Strain}_{x,y,z}$ = 0.018, 0.010, and 0.0098; $A_{x,y,z}$ (^{14}N , nat. abundance) = 0, 53, 0 mT; peak-to-peak line width $lwpp$ = $1.0 + 0\text{ mT}$ (Gaussian + Lorentzian), mw freq = 9.31026 GHz, range = 290–350 G. Simulation parameters, 213 K: g_{iso} = 2.069; $g\text{Strain}_{\text{iso}}$ = 0.013; A (^{14}N , nat. abundance) = 18 mT; peak-to-peak line-width $lwpp$ = $2.1 + 1.0\text{ mT}$ (Gaussian + Lorentzian); mw freq = 9.30053 GHz; range = 300–340 mT.

Oxidation of $^{\text{A}}\text{Ni-NTMS}_2$ (4.8 mg, $9.1\text{ }\mu\text{mol}$) with $[\text{Fc}^{\text{r}}]\text{NTf}_2$ (4.8 mg, $8.7\text{ }\mu\text{mol}$) followed above procedure. Simulation parameters for $^{\text{A}}\text{Ni}(\text{NTMS}_2)(\kappa\text{-O-N}(\text{SO}_2\text{CF}_3)_2)$ (Figure S8): g_{xy} = 2.434, 2.307, g_z masked by primary product; $g\text{Strain}_{xy}$ = 0.029 and 0.017; peak-to-peak line width $lwpp$ = $1.5 + 0\text{ mT}$ (Gaussian + Lorentzian); rel. abundance 0.13; mw freq = 9.311058 GHz; range = 260–350 G.

Vis–NIR spectroscopic monitoring the oxidation of $^{\text{A}}\text{Ni-NTMS}_2$ was carried out as follows. A quartz glass cuvette (1 cm) was charged with CH_2Cl_2 (2.6 mL), and reference spectra were recorded at T = 20, -20 , -40 , and $-60\text{ }^{\circ}\text{C}$. A 50 μL aliquot of a stock solution of $^{\text{A}}\text{Ni-NTMS}_2$ (5 mg, $9\text{ }\mu\text{mol}$) in CH_2Cl_2 (1.0 mL) was added, and spectra were recorded at the above temperatures for fitting the temperature dependence of sample concentration. A 83 μL aliquot of a stock solution of $[(4\text{-BrC}_6\text{H}_4)_3\text{N}]\text{BAR}^{\text{F}_4}$ (2.5 mg, $1.9\text{ }\mu\text{mol}$) in CH_2Cl_2 (2.0 mL), equal to 0.33 equiv of oxidant, was added in three successive steps at $-60\text{ }^{\circ}\text{C}$ and spectra were recorded each time. Finally, excess 5 μL of oxidant stock solution were added. Spectra were corrected for blank solvent background and are plotted in Figure S5; vis bands ($-60\text{ }^{\circ}\text{C}$): λ ($\epsilon/10^3/\text{M}^{-1}\text{ cm}^{-1}$) = 446 (2.5), 504 (2.7), 637 (2.2) nm.

In Situ Oxidation of $^{\text{A-O}}\text{Ni-NTMS}_2$. The procedure was the same as described for $^{\text{A}}\text{Ni-NTMS}_2$, except for the following changes: $^{\text{A-O}}\text{Ni-NTMS}_2$ (3 mg, $5\text{ }\mu\text{mol}$) in toluene (2.2 g), $[(4\text{-BrC}_6\text{H}_4)_3\text{N}]\text{BAR}^{\text{F}_4}$ (7 mg, $5\text{ }\mu\text{mol}$) in CH_2Cl_2 (2.0 mL). Figures S9 and S10 provide details for X-band cw-EPR spectra at 100 and 213 K, respectively. Simulation parameters, 100 K: Minor component $[(\kappa^3\text{-N,N',O}^*)\text{Ni-NTMS}_2]\text{BAR}^{\text{F}_4}$, $g_{x,y,z}$ = 2.046, 2.026, and 2.015; $g\text{Strain}_{x,y,z}$ = 0.005, 0.005, and 0.003; peak-to-peak line width $lwpp$ = $1.0 + 0\text{ mT}$ (Gaussian + Lorentzian); $A_{x,y,z}$ (^{14}N , nat. abundance) = 0, 0, 0 MHz; rel. abundance = 1.0; major component $[(\kappa^3\text{-N,N',O}^*)\text{Ni}(\text{NTMS}_2)]\text{BAR}^{\text{F}_4}$: $g_{x,y,z}$ = 2.057, 2.043, and 2.002;

$g\text{Strain}_{x,y,z}$ = 0.015, 0.006, and 0.003; peak-to-peak line width $lwpp$ = $1.0 + 0\text{ mT}$ (Gaussian + Lorentzian); $A_{x,y,z}$ (^{14}N , nat. abundance) = 0, 0, 0 MHz; rel. abundance = 1.5; mw freq = 9.30774 GHz; range = 310–340 mT. Simulation parameters, 213 K, $[(\kappa^3\text{-N,N',O}^*)\text{Ni-NTMS}_2]\text{BAR}^{\text{F}_4}$: g_{iso} = 2.029; $g_{\text{iso}}\text{Strain}$ = 0.001; peak-to-peak line width $lwpp$ = $0.9 + 0\text{ mT}$ (Gaussian + Lorentzian); A_{iso} (^{14}N ; nat. abundance) = 0 MHz; $[(\kappa^3\text{-N,N',O}^*)\text{Ni}(\text{NTMS}_2)]\text{BAR}^{\text{F}_4}$: g_{iso} = 2.033; $g\text{Strain}_{\text{iso}}$ = 0.001; peak-to-peak $lwpp$ = $0.9 + 0\text{ mT}$ (Gaussian + Lorentzian); A_{iso} (^{14}N ; nat. abundance) = 0 MHz; rel. abundances 1.0/1.0; mw freq = 9.294284 GHz; range = 310–340 mT.

In Situ Oxidation of $^{\text{A}}\text{Ni-SARTip}_2$. The procedure was the same as described for $^{\text{A}}\text{Ni-NTMS}_2$, except for the following changes: $^{\text{A}}\text{Ni-SARTip}_2$ (3.5 mg, $4.0\text{ }\mu\text{mol}$) in toluene (1.74 g), $[(4\text{-BrC}_6\text{H}_4)_3\text{N}]\text{BAR}^{\text{F}_4}$ (5.4 mg, $4.0\text{ }\mu\text{mol}$) in CH_2Cl_2 (2.0 mL). Figure S11 provides details for X-band cw-EPR spectrum at 100 K. Simulation parameters for major component: $g_{x,y,z}$ = 2.272, 2.099, and 2.052; $g\text{Strain}_{x,y,z}$ = 0.017, 0.018, and 0.009; peak-to-peak line width $lwpp$ = $2.0 + 0\text{ mT}$ (Gaussian + Lorentzian); mw freq. = 9.312679 GHz; range = 270–350 mT.

Computational Details. Electronic structure calculations were carried out through DFT methods using the ORCA program package.⁵⁸ For all optimizations, triple- ξ -valence TZVP⁵⁹ basis sets were used with the generalized gradient approximated functional BP86.⁶⁰ Pertinent metrical data is arranged in Tables S1–S3. Molecular orbitals and electronic properties were extracted from single-point calculations in the optimized geometries with the global hybrid functional TPSSH⁶¹ and triple- ξ -valence TZVP basis sets. Grimme's third-generation D3 correction of dispersion was applied,^{62,63} and medium effects were approximated in a dielectric continuum approach (COSMO), parametrized for THF.⁶⁴ Cartesian coordinates of the DFT optimized structures are assembled in form of a separate .xyz file (Supporting Information); frontier molecular orbital landscapes are shown in Figures 6–8. For each complex, the 60–80 lowest optical electronic transitions were assessed with ORCA-implemented TD-DFT methods within the Tamm–Dancoff approximation.

■ ASSOCIATED CONTENT

Supporting Information

The Supporting Information is available free of charge at <https://pubs.acs.org/doi/10.1021/acs.organomet.1c00121>.

General information on preparation/purification of proligands $^{\text{C/B}}\text{O-OPiv}$, reagents, solvents, additional UV/vis and IR absorption, and EPR spectroscopic, XRD and electrochemical data (PDF)

DFT optimized molecular structure data (XYZ)

Accession Codes

CCDC 2060407–2060410 contain the supplementary crystallographic data for this paper. These data can be obtained free of charge via www.ccdc.cam.ac.uk/data_request/cif, or by emailing data_request@ccdc.cam.ac.uk, or by contacting The Cambridge Crystallographic Data Centre, 12 Union Road, Cambridge CB2 1EZ, UK; fax: +44 1223 336033.

■ AUTHOR INFORMATION

Corresponding Author

Andreas Berkefeld – Institut für Anorganische Chemie, Eberhard Karls Universität Tübingen, 72076 Tübingen, Germany; orcid.org/0000-0002-2757-7841; Email: andreas.berkefeld@uni-tuebingen.de

Authors

Riyadh Alrefai – Institut für Anorganische Chemie, Eberhard Karls Universität Tübingen, 72076 Tübingen, Germany
Gerald Hörner – Anorganische Chemie IV, Universität Bayreuth, 95440 Bayreuth, Germany

Hartmut Schubert – Institut für Anorganische Chemie,
Eberhard Karls Universität Tübingen, 72076 Tübingen,
Germany

Complete contact information is available at:
<https://pubs.acs.org/10.1021/acs.organomet.1c00121>

Notes

The authors declare no competing financial interest.

ACKNOWLEDGMENTS

A.B. acknowledges Dr. Wolfgang Leis, Universität Tübingen, for recording emission spectroscopic data, Deutsche Forschungsgemeinschaft (DFG; German Research Foundation) for financial support of this work (grant number BE4424/7-1), and SCION-Syn GmbH & Co. KG, Schonungen, Germany, for the generous donation of 1,1,2,2,3,3-hexamethylindane-5,6-diamine. The CryoProbe Prodigy BBO NMR probe head used in this work was purchased with the support of an instrumentation program by the DFG, grant number INST 37/929-1 FUGG. A.B. dedicates this work to Prof. Dr. Wolfgang Kaim on the occasion of his 70th birthday. Herzlichen Glückwunsch!

REFERENCES

- (1) Tang, C. W.; VanSlyke, S. A. Organic electroluminescent diodes. *Appl. Phys. Lett.* **1987**, *51*, 913–915.
- (2) Tang, C. W.; VanSlyke, S. A.; Chen, C. H. Electroluminescence of doped organic thin films. *J. Appl. Phys.* **1989**, *65*, 3610–3616.
- (3) Yersin, H.; Rausch, A. F.; Czerwieńiec, R.; Hofbeck, T.; Fischer, T. The triplet state of organo-transition metal compounds. Triplet harvesting and singlet harvesting for efficient OLEDs. *Coord. Chem. Rev.* **2011**, *255*, 2622–2652.
- (4) Shaw, M. H.; Twilton, J.; MacMillan, D. W. C. Photoredox Catalysis in Organic Chemistry. *J. Org. Chem.* **2016**, *81*, 6898–6926.
- (5) Prier, C. K.; Rankic, D. A.; MacMillan, D. W. C. Visible Light Photoredox Catalysis with Transition Metal Complexes: Applications in Organic Synthesis. *Chem. Rev.* **2013**, *113*, 5322–5363.
- (6) Milligan, J. A.; Phelan, J. P.; Badir, S. O.; Molander, G. A. Alkyl Carbon–Carbon Bond Formation by Nickel/Photoredox Cross-Coupling. *Angew. Chem., Int. Ed.* **2019**, *58*, 6152–6163.
- (7) Welin, E. R.; Le, C.; Arias-Rotondo, D. M.; McCusker, J. K.; MacMillan, D. W. C. Photosensitized, energy transfer-mediated organometallic catalysis through electronically excited nickel(II). *Science* **2017**, *355*, 380.
- (8) Haque, A.; Xu, L.; Al-Balushi, R. A.; Al-Suti, M. K.; Ilimi, R.; Guo, Z.; Khan, M. S.; Wong, W.-Y.; Raithby, P. R. Cyclometalated tridentate platinum(II) acrylate complexes: old wine in new bottles. *Chem. Soc. Rev.* **2019**, *48*, 5547–5563.
- (9) Ibrahim-Ouali, M.; Dumur, F. Recent Advances on Metal-Based Near-Infrared and Infrared Emitting OLEDs. *Molecules* **2019**, *24*, 1412.
- (10) Cebrián, C.; Mauro, M. Recent advances in phosphorescent platinum complexes for organic light-emitting diodes. *Beilstein J. Org. Chem.* **2018**, *14*, 1459–1481.
- (11) Longhi, E.; De Cola, L. Iridium(III) Complexes for OLED Application. *Iridium(III) in Optoelectronic and Photonics Applications* **2017**, 205–274.
- (12) Dorn, M.; Kalmbach, J.; Boden, P.; Pöpcke, A.; Gómez, S.; Förster, C.; Kuczelin, F.; Carrella, L. M.; Büldt, L. A.; Bings, N. H.; Rentschler, E.; Lochbrunner, S.; González, L.; Gerhards, M.; Seitz, M.; Heinze, K. A Vanadium(III) Complex with Blue and NIR-II Spin-Flip Luminescence in Solution. *J. Am. Chem. Soc.* **2020**, *142*, 7947–7955.
- (13) Wenger, O. S. Photoactive Complexes with Earth-Abundant Metals. *J. Am. Chem. Soc.* **2018**, *140*, 13522–13533.
- (14) Hockin, B. M.; Li, C.; Robertson, N.; Zysman-Colman, E. Photoredox catalysts based on earth-abundant metal complexes. *Catal. Sci. Technol.* **2019**, *9*, 889–915.
- (15) Kjær, K. S.; Kaul, N.; Prakash, O.; Chábera, P.; Rosemann, N. W.; Honarfar, A.; Gordivska, O.; Fredin, L. A.; Bergquist, K.-E.; Häggström, L.; Ericsson, T.; Lindh, L.; Yartsev, A.; Styring, S.; Huang, P.; Uhlig, J.; Bendix, J.; Strand, D.; Sundström, V.; Persson, P.; Lomoth, R.; Wärnmark, K. Luminescence and reactivity of a charge-transfer excited iron complex with nanosecond lifetime. *Science* **2019**, *363*, 249.
- (16) Williams, J. A. G. The coordination chemistry of dipyritylbenzene: N-deficient terpyridine or panacea for brightly luminescent metal complexes? *Chem. Soc. Rev.* **2009**, *38*, 1783–1801.
- (17) Dixon, I. M.; Alary, F.; Boggio-Pasqua, M.; Heully, J.-L. Reversing the relative 3MLCT–3MC order in Fe(II) complexes using cyclometalating ligands: a computational study aiming at luminescent Fe(II) complexes. *Dalton Trans.* **2015**, *44*, 13498–13503.
- (18) Mukherjee, S.; Torres, D. E.; Jakubikova, E. HOMO inversion as a strategy for improving the light-absorption properties of Fe(II) chromophores. *Chem. Sci.* **2017**, *8*, 8115–8126.
- (19) Braun, J. D.; Lozada, I. B.; Kolodziej, C.; Burda, C.; Newman, K. M. E.; van Lierop, J.; Davis, R. L.; Herbert, D. E. Iron(II) coordination complexes with panchromatic absorption and nanosecond charge-transfer excited state lifetimes. *Nat. Chem.* **2019**, *11*, 1144–1150.
- (20) Braun, J. D.; Lozada, I. B.; Herbert, D. E. In Pursuit of Panchromatic Absorption in Metal Coordination Complexes: Experimental Delineation of the HOMO Inversion Model Using Pseudo-Octahedral Complexes of Diarylamido Ligands. *Inorg. Chem.* **2020**, *59*, 17746–17757.
- (21) Sandleben, A.; Vogt, N.; Hörner, G.; Klein, A. Redox Series of Cyclometalated Nickel Complexes [Ni(R)Ph(R')bpy]^{+0/-2-} (H–(R)Ph(R')bpy = Substituted 6-Phenyl-2,2'-bipyridine). *Organometallics* **2018**, *37*, 3332–3341.
- (22) Kletsch, L.; Hörner, G.; Klein, A. Cyclometalated Ni(II) Complexes [Ni(NACAN)X] of the Tridentate 2,6-di(2-pyridyl)phenylidene Ligand. *Organometallics* **2020**, *39*, 2820–2829.
- (23) Wong, Y.-S.; Tang, M.-C.; Ng, M.; Yam, V. W.-W. Toward the Design of Phosphorescent Emitters of Cyclometalated Earth-Abundant Nickel(II) and Their Supramolecular Study. *J. Am. Chem. Soc.* **2020**, *142*, 7638–7646.
- (24) Sun, R.; Qin, Y.; Rucolo, S.; Schnedermann, C.; Costentin, C.; Nocera, D. G. Elucidation of a Redox-Mediated Reaction Cycle for Nickel-Catalyzed Cross Coupling. *J. Am. Chem. Soc.* **2019**, *141*, 89–93.
- (25) Ting, S. I.; Garakyaraghi, S.; Taliaferro, C. M.; Shields, B. J.; Scholes, G. D.; Castellano, F. N.; Doyle, A. G. 3d-d Excited States of Ni(II) Complexes Relevant to Photoredox Catalysis: Spectroscopic Identification and Mechanistic Implications. *J. Am. Chem. Soc.* **2020**, *142*, 5800–5810.
- (26) Wenger, O. S. Photoactive Nickel Complexes in Cross-Coupling Catalysis. *Chem. - Eur. J.* **2021**, *27*, 2270–2278.
- (27) Berkefeld, A.; Fröhlich, M.; Kordan, M.; Hörner, G.; Schubert, H. Selective metalation of phenol-type proligands for preparative organometallic chemistry. *Chem. Commun.* **2020**, *56*, 3987–3990.
- (28) Creutz, S. E.; Lotito, K. J.; Fu, G. C.; Peters, J. C. Photoinduced Ullmann C–N Coupling: Demonstrating the Viability of a Radical Pathway. *Science* **2012**, *338*, 647.
- (29) McGuire, R.; Wilson, M. H.; Nash, J. J.; Fanwick, P. E.; McMillin, D. R. Lewis Acid and Base Sensing by Platinum(II) Polypyridines. *Inorg. Chem.* **2008**, *47*, 2946–2948.
- (30) Nicholson, R. S.; Shain, I. Theory of Stationary Electrode Polarography. Single Scan and Cyclic Methods Applied to Reversible, Irreversible, and Kinetic Systems. *Anal. Chem.* **1964**, *36*, 706–723.
- (31) Stoll, S.; Schweiger, A. EasySpin, a comprehensive software package for spectral simulation and analysis in EPR. *J. Magn. Reson.* **2006**, *178*, 42–55.

- (32) Büttner, T.; Geier, J.; Frison, G.; Harmer, J.; Calle, C.; Schweiger, A.; Schönberg, H.; Grützmacher, H. A Stable Aminyl Radical Metal Complex. *Science* **2005**, *307*, 235.
- (33) Collins, T. J.; Nichols, T. R.; Uffelman, E. S. A square-planar nickel(III) complex of an innocent ligand system. *J. Am. Chem. Soc.* **1991**, *113*, 4708–4709.
- (34) Hanss, J.; Krüger, H.-J. First Isolation and Structural Characterization of a Nickel(III) Complex Containing Aliphatic Thiolate Donors. *Angew. Chem., Int. Ed.* **1998**, *37*, 360–363.
- (35) Jacobs, S. A.; Margerum, D. W. Solution properties of bis(dipeptide)nickelate(III) complexes and kinetics of their decomposition in acid. *Inorg. Chem.* **1984**, *23*, 1195–1201.
- (36) Thomas, F. Ligand-centred oxidative chemistry in sterically hindered salen complexes: an interesting case with nickel. *Dalton Trans.* **2016**, *45*, 10866–10877.
- (37) Kurz, H.; Schötz, K.; Papadopoulos, I.; Heinemann, F. W.; Maid, H.; Guldi, D. M.; Köhler, A.; Hörner, G.; Weber, B. A Fluorescence-Detected Coordination-Induced Spin State Switch. *J. Am. Chem. Soc.* **2021**, *143*, 3466–3480.
- (38) Mandapati, P.; Giesbrecht, P. K.; Davis, R. L.; Herbert, D. E. Phenanthridine-Containing Pincer-like Amido Complexes of Nickel, Palladium, and Platinum. *Inorg. Chem.* **2017**, *56*, 3674–3685.
- (39) Klein, A.; Hurkes, N.; Kaiser, A.; Wielandt, W. π -Stacking Modulates the Luminescence of [(dppz)Ni(Mes)Br] (dppz = dipyrido[3,2-a:2',3'-c]phenazine, Mes = 2,4,6-trimethylphenyl). *Z. Anorg. Allg. Chem.* **2007**, *633*, 1659–1665.
- (40) Lazzaro, D. P.; McGuire, R.; McMillin, D. R. Regiospecific Quenching of a Photoexcited Platinum(II) Complex at Acidic and Basic Sites. *Inorg. Chem.* **2011**, *50*, 4437–4444.
- (41) Kaim, W. Electron transfer to 1,10-phenanthroline by grignard reagents: the spin distribution in organomagnesium radical complexes. *J. Organomet. Chem.* **1981**, *222*, c17–c20.
- (42) Kaim, W. Electron transfer to complex ligands. Radical anions and organomagnesium radical complexes of 2,2'-bipyridines and 1,10-phenanthrolines. *J. Am. Chem. Soc.* **1982**, *104*, 3833–3837.
- (43) Fees, J.; Kaim, W.; Moscherosch, M.; Matheis, W.; Klima, J.; Krejcik, M.; Zalis, S. Electronic structure of the "molecular light switch" bis(bipyridine)dipyrido[3,2-a:2',3'-c]phenazineruthenium-(2+). Cyclic voltammetric, UV/visible and EPR/ENDOR study of multiply reduced complexes and ligands. *Inorg. Chem.* **1993**, *32*, 166–174.
- (44) Schoonover, J. R.; Bates, W. D.; Meyer, T. J. Application of Resonance Raman Spectroscopy to Electronic Structure in Metal Complex Excited States. Excited-State Ordering and Electron Delocalization in Dipyrido[3,2-a:2',3'-c]phenazine (dppz): Complexes of Re(I) and Ru(II). *Inorg. Chem.* **1995**, *34*, 6421–6422.
- (45) Butsch, K.; Gust, R.; Klein, A.; Ott, I.; Romanski, M. Tuning the electronic properties of dppz-ligands and their palladium(ii) complexes. *Dalton Trans.* **2010**, *39*, 4331–4340.
- (46) Delaney, S.; Pascaly, M.; Bhattacharya, P. K.; Han, K.; Barton, J. K. Oxidative Damage by Ruthenium Complexes Containing the Dipyridophenazine Ligand or Its Derivatives: A Focus on Intercalation. *Inorg. Chem.* **2002**, *41*, 1966–1974.
- (47) Wang, C.; Otto, S.; Dorn, M.; Kreidt, E.; Lebon, J.; Sršan, L.; Di Martino-Fumo, P.; Gerhards, M.; Resch-Genger, U.; Seitz, M.; Heinze, K. Deuterated Molecular Ruby with Record Luminescence Quantum Yield. *Angew. Chem., Int. Ed.* **2018**, *57*, 1112–1116.
- (48) Nguyen, T.; Panda, A.; Olmstead, M. M.; Richards, A. F.; Stender, M.; Brynda, M.; Power, P. P. Synthesis and Characterization of Quasi-Two-Coordinate Transition Metal Dithiolates M(SAr*)₂ (M = Cr, Mn, Fe, Co, Ni, Zn; Ar* = C₆H₃-2,6(C₆H₂-2,4,6-¹Pr)₂). *J. Am. Chem. Soc.* **2005**, *127*, 8545–8552.
- (49) Adhikari, D.; Mossin, S.; Basuli, F.; Huffman, J. C.; Szilagy, R. K.; Meyer, K.; Mindiola, D. J. Structural, Spectroscopic, and Theoretical Elucidation of a Redox-Active Pincer-Type Ancillary Applied in Catalysis. *J. Am. Chem. Soc.* **2008**, *130*, 3676–3682.
- (50) Mankad, N. P.; Antholine, W. E.; Szilagy, R. K.; Peters, J. C. Three-Coordinate Copper(I) Amido and Aminyl Radical Complexes. *J. Am. Chem. Soc.* **2009**, *131*, 3878–3880.
- (51) Roberts, B. P. Polarity-reversal catalysis of hydrogen-atom abstraction reactions: concepts and applications in organic chemistry. *Chem. Soc. Rev.* **1999**, *28*, 25–35.
- (52) Kaupp, M. The role of radial nodes of atomic orbitals for chemical bonding and the periodic table. *J. Comput. Chem.* **2007**, *28*, 320–325.
- (53) Mews, N. M.; Berkefeld, A.; Hörner, G.; Schubert, H. Controlling Near-Infrared Chromophore Electronic Properties through Metal–Ligand Orbital Alignment. *J. Am. Chem. Soc.* **2017**, *139*, 2808–2815.
- (54) Rosokha, S. V.; Stern, C. L.; Ritzert, J. T. π -Bonded molecular wires: self-assembly of mixed-valence cation-radical stacks within the nanochannels formed by inert tetrakis[3,5-bis(trifluoromethyl)phenyl]borate anions. *CrystEngComm* **2013**, *15*, 10638–10647.
- (55) Wannagat, U.; Niederprüm, H. Beiträge zur Chemie der Silicium-Stickstoff-Verbindungen, XIII. Silylsubstituierte Alkaliamide. *Chem. Ber.* **1961**, *94*, 1540–1547.
- (56) Bailey, P. J.; Coxall, R. A.; Dick, C. M.; Fabre, S.; Henderson, L. C.; Herber, C.; Liddle, S. T.; Loroño-González, D.; Parkin, A.; Parsons, S. The First Structural Characterisation of a Group 2 Metal Alkylperoxide Complex: Comments on the Cleavage of Dioxygen by Magnesium Alkyl Complexes. *Chem. - Eur. J.* **2003**, *9*, 4820–4828.
- (57) Niemeyer, M.; Power, P. P. Donor-Free Alkali Metal Thiolates: Synthesis and Structure of Dimeric, Trimeric, and Tetrameric Complexes with Sterically Encumbered Terphenyl Substituents. *Inorg. Chem.* **1996**, *35*, 7264–7272.
- (58) Neese, F. The ORCA program system. *Wiley Interdiscip. Rev.: Comput. Mol. Sci.* **2012**, *2*, 73–78.
- (59) Schäfer, A.; Horn, H.; Ahlrichs, R. Fully optimized contracted Gaussian basis sets for atoms Li to Kr. *J. Chem. Phys.* **1992**, *97*, 2571–2577.
- (60) Becke, A. D. Density-functional exchange-energy approximation with correct asymptotic behavior. *Phys. Rev. A: At., Mol., Opt. Phys.* **1988**, *38*, 3098–3100.
- (61) Staroverov, V. N.; Scuseria, G. E.; Tao, J.; Perdew, J. P. Comparative assessment of a new nonempirical density functional: Molecules and hydrogen-bonded complexes. *J. Chem. Phys.* **2003**, *119*, 12129–12137.
- (62) Grimme, S.; Antony, J.; Ehrlich, S.; Krieg, H. A consistent and accurate ab initio parametrization of density functional dispersion correction (DFT-D) for the 94 elements H-Pu. *J. Chem. Phys.* **2010**, *132*, 154104.
- (63) Grimme, S.; Ehrlich, S.; Goerigk, L. Effect of the damping function in dispersion corrected density functional theory. *J. Comput. Chem.* **2011**, *32*, 1456–1465.
- (64) Klamt, A.; Schüürmann, G. COSMO: a new approach to dielectric screening in solvents with explicit expressions for the screening energy and its gradient. *J. Chem. Soc., Perkin Trans. 2* **1993**, 799–805.